Modeling nanoparticle charge distribution in the afterglow of non-thermal plasmas and comparison with measurements

Vikram Suresh[#], Li Li[#], Joshua Redmond Go Felipe & Ranganathan Gopalakrishnan[*]
Department of Mechanical Engineering, The University of Memphis, Memphis TN, USA

Submitted to:

Journal of Physics D: Applied Physics

[#]Equally contributing authors
*Corresponding author: rgplkrsh@memphis.edu;
Tel: 1-626-319-6187, Fax: 1-901-678-4180

Abstract

Particle charging in the afterglows of non-thermal plasmas typically take place in a non-neutral space charge environment. We model the same by incorporating particle-ion collision rate constant models, developed in prior work by analyzing particle-ion trajectories calculated using Langevin Dynamics simulations, into species transport equations for ions, electrons and charged particles in the afterglow. A scaling analysis of particle charging and additional Langevin Dynamics calculations of the particle-ion collision rate constant are presented to extend the range of applicability to ion electrostatic to thermal energy ratios of 300 and diffusive Knudsen number (that scales inversely with gas pressure) up to 2000. The developed collision rate constant models are first validated by comparing predictions of particle charge against measured values in a stationary, non-thermal DC plasma from past PK-4 campaigns published in Phys. Rev. Lett. 93(8): 085001 and Phys. Rev. E 72(1): 016406). The comparisons reveal excellent agreement within $\pm 35\%$ for particles of radius $0.6,1.0,1.3\ \mu m$ in the gas pressure range of $\sim 20 - 150\ Pa$. The experiments to probe particle charge distributions by Sharma et al. (J. Physics D: Appl. Phys. 53(24): 245204) are modeled using the validated particle-ion collision rate constant models and the calculated charge fractions are compared with measurements. The comparisons reveal that the ion/electron concentration and gas temperature in the afterglow critically influence the particle charge and the predictions are generally in qualitative agreement with the measurements. Along with critical assessment of the modeling assumptions, several recommendations are presented for future experimental design to probe charging in afterglows.

1. Introduction

Non-thermal dusty plasmas (i.e.) weakly ionized gas discharges are two-temperature systems that contain energetic electrons that are much hotter than the ions and background gas molecules, with energies typically on the order of $k_B T_e \sim 0.1 - 10\ eV$ and $k_B T_i \sim 0.03 - 0.05\ eV$ and gas pressures $p_g \sim 10^2 - 10^5\ Pa$. A key advantage of *non-thermal dusty plasmas* is their relatively low operating temperatures $(< 500\ K)$ combined with the presence of energetic electrons whose temperature is on the order of $\sim 10{,}000\ K$, a combination that creates novel pathways for particle growth dynamics and surface chemistry[1-3], generally inaccessible via colloidal or aerosol routes. Flow-through non-thermal plasmas, distinct from stationary plasmas formed inside a sealed chamber and a stagnant gas, are effective vehicles for materials synthesis/processing[4,5] as they allow the chemical transformation and nucleation of precursor vapors, followed by grain growth via coagulation[6-8] to produce desired aerosol size distribution, shape, composition and crystalline phase in materials while being amenable to online, real-time optical diagnostics[9] and aerosol electrical mobility analysis[10-13]. While the non-thermal plasma itself is spatially well-defined by the creation of energetic species due to the influx of power through electrodes or irradiation, the produced species are not necessarily completely reacted away within the axial extent of the cylindrical flow reactor. The penetration depth of the plasma-generated species (ions, electrons, free radicals) transported by the gas flow to downstream axial locations, known as the *afterglow*, is determined by the gas flowrate and temperature, diffusivity of the charged species and rates of chemical reactions that act as sinks for the plasma-generated species. Here, we distinguish between *spatial* afterglows formed downstream of flow-through plasmas from the term *temporal* afterglows[14-20] that is used to describe the decay of charged species over time by recombination and diffusion in the space after the external power input to a plasma is turned off. Among other attributes, the electrical charge of aerosol particles produced in or flown through a non-thermal plasma strongly influences their subsequent growth dynamics[2,4,21]. Recent investigation by Minderhout et al.[22] reports particle charging measurements in a combination of temporal and spatial afterglows. The particle charge is modified both in the *active plasma* region by the nearly neutral space charge environment $(n_i \cong n_e)$ wherein ion-electron pair production rate by ionization balances the losses due to recombination, diffusional deposition on surfaces and collisional charging of particles, and, by the non-neutral, positive space charge in the *spatial afterglow* region $(n_i > n_e)$ where electrons are lost at much higher rates than ions without replenishment by ionization; n_i is the ion number concentration and n_e is the electron number concentration. Motivated by recent experimental investigations of charging in the spatial afterglow downstream of non-thermal plasmas to infer the particle charge distribution[23,24] as well as to propose charge control technologies[25,26], we describe a modeling approach to calculate the charge distribution f_p of aerosol particles flown

through a non-thermal plasma and the afterglow; f_p is the fraction of particles carrying p charges in a population of monodisperse aerosol particles. Modeling and tuning f_p as a function of particle size and other plasma attributes accurately is needed for the selection of materials synthesis plasma process parameters in order to obtain tight control over the particle size distribution via collisional growth[27-34], prevent undesirable agglomeration by unipolar charging[35-38] as well as the promote desirable production of fractal aggregates by scavenging of non-negatively charged monomers by negatively charged larger particles[11,27].

In the plasma region, a suitably measured or estimated n_i, n_e (considered to be nearly spatially uniform) may be used to obtain the charge $\bar{z}_p$ by equating the (positive) ion and (negative) electron currents to a particle same from a stationary (non-drifting) plasma. The PK-4 experimental campaigns[39-41] show that $a_p \sim 0.6 - 1.3\ \mu m$-sized spherical dust particles attain a steady state charge of $\sim 10^2 - 10^4$ units of elementary negative charge in *stationary* non-thermal DC plasmas at pressures $\sim 20 - 500\ Pa$ in argon gas; $a_p = \frac{d_p}{2}$ and d_p is the diameter of a spherical particle. For *flow-through* plasmas, the particle charge distribution f_p, in the limit of particle residence time in the plasma region t_r being much longer than the characteristic time τ for particle-ion and particle-electron collisions $(t_r \gg \tau)$, presumably attains a steady state with a nominally negative mean charge $\left(\sum_{p=-\infty}^{\infty} f_p p \equiv \bar{z}_p < 0\right)$ owing to higher mobility of electrons than ions $(\mu_e > \mu_i)$. For $d_p > 20\ nm$, $\left|\bar{z}_p\right| \sim 10^2 - 10^4$ and the width $\sigma_p \equiv \left(\sum_{p=-\infty}^{\infty} f_p \left(p - \bar{z}_p\right)^2\right)^{\frac{1}{2}}$ of the charge distribution is usually neglected when compared to $\left|\bar{z}_p\right|$ and the particle charge is considered to be a mono-valued quantity: $\sigma_p \ll \left|\bar{z}_p\right|$. For $d_p < 20\ nm$-sized particles, $|\bar{z}_p| \sim 10$ and consequently, it is important to consider the finite width of the charge distribution that is comparable to the mean value: $\sigma_p \sim \left|\bar{z}_p\right|$. Further, for $d_p < 2\ nm$-sized freshly nucleated particles inside the plasma, particle charge can also be non-negative (i.e.) $z_p \geq 0$. The presence of non-negatively charged particles is key to the scavenging of small particles by larger, negatively charged particles to sustain the growth of particles to larger sizes[4,42-45].

In contrast to the plasma region, due to the longer extinction time of the ions than electrons, particle charging in the spatial afterglow proceeds predominantly by attachment of (positive) ions $(z_i = +1)$ to particles through combined diffusional and electrostatic motion leading to increase of particle charge: $p \rightarrow p + z_i$, leading to the formation of bipolar or even solely positively charged particles[23,24] starting from initially negative particles leaving the active plasma region. Modeling the charge distribution of particles f_p exiting the afterglow region is more challenging than calculating the particle charge inside the (stationary) plasma region for at least three reasons: Firstly, the afterglow's boundary

is not precisely delineated and the spatial decay of ions along the axis must be properly accounted for while estimating particle charge[24]; this requires accurate measurement of the gas flow rate Q and axial temperature profile $T(z)$ in the afterglow region. A suitable fluid model of the decay of the spatial concentration of ions $\langle n_i(z)\rangle_r$ and electrons $\langle n_e(z)\rangle_r$ as a function of the axial location needs to be coupled to a calculation of f_p to properly account for the variation in ion and electron currents to a particle; $\langle\cdot\rangle_r$ denotes averaging over the radial cross-section at a given axial location z. Secondly, the contribution of particle-ion combined Coulomb and *image* potential interactions must be taken into account for collisions between particles[46-50] whose charge is comparable to 0: $z_p \sim 0$. Barring a few exceptions[46,51,52], the contribution of the image potential to the charging of particles in plasmas have been largely ignored in instances where $-z_p \gg 0$ but are routinely accounted for in aerosol particle diffusion charging modeling[49,50,53-60] where charge levels are closer to 0: $z_p \sim [-20,20]$. Lastly, the prediction of f_p also requires that the charge of particles leaving the plasma region is calculated or measured accurately to serve as an initial condition for the modeling in the afterglow region.

Particle charge may be calculated by balancing of the production and consumption of positively and negatively charged particles in a plasma at steady state $(t_r \ll \tau)$. The rate of collisions between a particle carrying p charges and an ion is calculated as: $R_{pi} = \beta(p,i)n_p n_i$; $\beta(p,i)$ is the particle-ion collision rate constant that is calculated from theoretical models of charging, commonly referred to as the ion-flux coefficient in the plasma literature and as the particle-ion collision kernel in the aerosol literature, and n_p is the number concentration of particles carrying p charges. Likewise, the particle-electron collision rate is also calculated as $R_{pe} = \beta(p,e)n_p n_e$; $\beta(p,e)$ is the particle-electron collision rate constant. The particle charge distribution $f_p = \frac{n_p}{\sum_{p=-\infty}^{p=+\infty} n_p}$ on a population of mono-sized particles of diameter d_p are obtained by solving a system of algebraic equations:

$$0 = -\beta(p,i)n_p n_i - \beta(p,e)n_p n_e + \beta(p-1,i)n_{p-1}n_i + \beta(p+1,e)n_{p+1}n_e \ldots (1)$$

In a stationary plasma, species concentrations are assumed to spatially homogenous to derive a 0-D model for simplicity. Due to much smaller electron-neutral collision cross-sections compared to ions and neutrals $(\sigma_{en} \ll \sigma_{in})$, even at atmospheric pressures $(\sim 10^5\ Pa)$, particle-electron collisions may be considered to be collisionless and $\beta(p,e)$ is described by the collisionless orbital motion-limited (OML) model[61,62], derived for collisions in vacuum. Among the instances that could lead to significant deviation of $\beta(p,i)$ from OML predictions, Goree [63] recognizes ion-neutral gas molecule collisions at finite gas pressures as a reason for the increase in ion currents collected by particles due to trapping of low energy ions[64]. The effect of ion-neutral collisions has been a subject of

numerous theoretical investigations both in the context of aerosol charging[55-58,60,65-68] as well as particle charging in dusty plasmas[69-87] as summarized by Chahl and Gopalakrishnan [65]. In addition to ion-neutral collisions, flow-through plasmas also present the challenge of spatially varying ion, electron and particle concentrations as described before, that may be modeled by considering coupled species transport equations at steady state ($t_r \gg \tau$):

$$0 = \nabla \cdot \left(-D_i \nabla n_i + \vec{u}_g n_i\right) - R_{ie} - \sum_{p=-\infty}^{p=+\infty} \beta(p,i) n_p n_i \ldots (2a)$$

$$0 = \nabla \cdot \left(-D_e \nabla n_e + \vec{u}_g n_e\right) - R_{ie} - \sum_{p=-\infty}^{p=+\infty} \beta(p,e) n_p n_e \ldots (2b)$$

$$0 = \nabla \cdot \left(-D_p \nabla n_p + \vec{u}_g n_p\right) - \beta(p,i) n_p n_i - \beta(p,e) n_p n_e + \beta(p-1,i) n_{p-1} n_i + \beta(p+1,e) n_{p+1} n_e \ldots (2c)$$

D_i, D_e, D_p are, respectively, the diffusion constants of the ion, electron and particles and R_{ie} is the gas-phase ion-electron recombination rate. The gas flow field $\vec{u}_g$ may be considered to be one-way coupled to the species transport equations above and is taken independently to be a simple plug flow model. Calculating the gas temperature profile T_g is considerably more complex as it requires an estimate of the power injected into the gas flow by the plasma. For simplicity, a constant gas temperature is assumed or T_g measured at several axial locations along the plasma reactor may be used as an empirical substitute. In this article, we employ an experimentally validated model of $\beta(p,i)$ developed for the diffusion charging of spherical[57] as well as arbitrary shaped[56] aerosol particles by parameterizing the particle-ion collision time distributions calculated using Langevin Dynamics (LD) simulations[65]. Among available $\beta(p,i)$ models, the LD-based approach of Chahl and Gopalakrishnan [65] is chosen for the excellent agreement (within $\pm 30\%$ nominally) that it yields with experimental data for a wide range of aerosol charging conditions (gas pressure, temperature, ion mass and electrical mobility, particle size and shape) and convergence to known analytical expressions in the continuum (high pressure) and free molecular (low pressure or vacuum) limits. The reminder of the article is organized as follows: As the details of $\beta(p,i)$ model development using LD simulations are explained in prior work[56-59,65,88,89], as part of our *Methods*, we only present a scaling analysis of particle charging in plasmas and describe additional LD simulation results to expand the applicability the model of Chahl and Gopalakrishnan [65] that was derived to describe $\beta(p,i)$ for highly charged $\left(-z_p \gg 0\right)$ particles and ions interacting through a screened Coulomb potential: $\Phi = \frac{z_p z_i e^2}{4\pi\varepsilon_0 r} e^{-\frac{r}{\lambda_D}}$; r is the particle-ion distance and $\lambda_D = \left(\frac{\varepsilon_0 k_B T_i}{n_i e^2}\right)^{1/2}$ is the Debye screening length based on the ion concentration. An experimental

validation of $\beta(p,i)$ for highly charged particles is provided by comparing predictions of mean charge $\bar{z}_p$ with corresponding experimental data reported by the PK-4 grain charging experiments in DC plasmas[40,41]. To describe the charging of particles at lower charge levels $(z_p \sim 0)$, we also summarize the $\beta(p,i)$ model put forth by Li et al. [57] that captures the combined Coulomb and image potential interaction: $\Phi = \frac{z_p z_i e^2}{4\pi\varepsilon_0 r} - \frac{\varepsilon_r - 1}{\varepsilon_r + 1}\frac{z_i^2 e^2}{4\pi\varepsilon_o}\frac{a_p^3}{2r^2(r^2 - a_p^2)}$; ε_r is the particle material dielectric constant. Further, we describe our solutions to eq. 2 while incorporating LD-based $\beta(p,i)$ models along with details of our modeling of the particle charge distribution measurements reported by Sharma et al. [23]. The *Results and Discussion* section presents our comparison between model predictions and experimental data and we attempt to critically assess the LD-based $\beta(p,i)$ model and its applicability for particle charging in afterglows. Therein, complexities of particle charging that are included and excluded in our modeling are discussed in detail. Finally, we present the *Conclusions* derived from this modeling study about the usage of LD-based $\beta(p,i)$ for describing particle charging in flow-through plasmas along with recommendations for future experimental investigations.

2. Scaling analysis of particle charging

The collision of positive ions with charged particles is modeled as a point mass ion (of mass m_i) colliding with a spherical particle of radius a_p including the effect of electrostatic interaction and the ion's thermal energy. At sufficiently low ion and grain concentrations, it may be reasonably assumed that grains and ions interact with each other while being nominally isolated (dilute, binary interactions). In lieu of two-way coupled determination of the electric potential (using the Poisson-Boltzmann equation) and the charge (ion/electron) concentration profile (taking into account drift and diffusion), the use of an *apriori* prescribed potential is commonly employed. While the rigorous justification of the *ad hoc* use of such a screened Coulomb is not available, it is seen from numerical[90] and theoretical[91] investigations that it nevertheless produces a close approximation of the grain-ion potential. Following prior theoretical developments[68,70,77], the nondimensional grain-ion interaction potential is taken to be $\frac{\varphi(r)}{k_B T_i} = -\frac{\Psi_E}{r}\exp\left(-\frac{r}{S_D}\right)$. Here, $\Psi_E = -\frac{z_p z_i e^2}{4\pi\varepsilon_o a_p k_B T_i}$ is the ratio of the nominal grain-ion electrostatic potential energy $-\frac{z_p z_i e^2}{4\pi\varepsilon_o a_p}$ to the ion thermal energy $k_B T_i$; $\Psi_E > 0$ represents collisions between a positive ion and a negatively charged particle and vice versa. The ion Debye screening length λ_D is normalized by the grain radius to obtain the non-dimensional screening length $S_D = \frac{\lambda_D}{a_p}$. In vacuum, OML model-derived $\beta(p,i)$ is:

$$\beta(p,i) = \left(\frac{8k_B T_i}{\pi m_i}\right)^{1/2} \pi a_p^2 \eta_f(\Psi_E, S_D) \ldots (3a)$$

Here, $\eta_f(\Psi_E, S_D)$ is the enhancement of the hard sphere grain-ion collision cross-section πa_p^2 due to grain-ion electrostatic interaction. By conserving momentum and kinetic energy of the ion approaching a stationary grain[61,62], $\eta_f(\Psi_E, S_D)$ is derived as:

$$\eta_f(\Psi_E, S_D) = \begin{cases} 1 + \Psi_E \exp\left(-\frac{1}{S_D}\right), \Psi_E \geq 0 \\ \exp\left(\Psi_E \exp\left(-\frac{1}{S_D}\right)\right), \Psi_E \leq 0 \end{cases} \ldots (3b)$$

Eq. 3 (3a and 3b) has been used at low pressures ($< 10\ Pa$) but has been shown to be inaccurate for $\sim 20 - 500\ Pa$ experimentally[39-41]. In the opposite limit of high pressures ($\sim 10^5\ Pa$), $\beta(p,i)$ is determined by continuum transport of ions due to mobility-limited electrostatic drift and thermal diffusion:

$$\beta(p,i) = 4\pi \frac{k_B T_i}{f_i} a_p \eta_c(\Psi_E, S_D) \ldots (4a)$$

Here, f_i is the ion friction factor that can be obtained from a measurement of the ion diffusion coefficient $D_i = \frac{k_B T_i}{f_i}$ or the low-field electrical mobility $\mu_i = \frac{z_i e}{f_i}$. $\eta_c(\Psi_E, S_D)$ is the continuum enhancement factor[68,92]:

$$\eta_c(\Psi_E, S_D) = \left(\int_1^\infty \frac{1}{r^2} \exp\left(-\frac{\Psi_E}{r} \exp\left(-\frac{r}{S_D} \right) \right) dr \right)^{-1} \ldots (4b)$$

In our analysis of positive ion current collected by a particle, we neglect the influence of any external fields. This assumption is consistent with the experimental studies of particle charging in stationary plasmas[40,41] and in flow-through plasmas selected for model validation[23]. Eq. 3 and eq. 4 present the vacuum/low-pressure and high-pressure limit of $\beta(p, i)$, respectively. At intermediate pressures ($\sim 10^2 - 10^5\ Pa$), Langevin Dynamics has been previously exploited to predict the steady-state mean charge on grains[66,93,94] and develop β_i models for aerosols and dusty plasmas[57,58,65,95,96]. As stated before, our first objective is to test the model for β_i developed by Chahl and Gopalakrishnan [65] against PK-4 grain charge measurements[39-41]. We briefly review the model developed by Chahl and Gopalakrishnan [65] before describing additional calculations performed in this work to extend their model beyond $\Psi_E = 60$ up to $\Psi_E \leq 300$.

Scaling of β_i with $\frac{a_p \eta_f(\Psi_E, S_D)}{\eta_c(\Psi_E, S_D)}$ as a reference length and $\frac{m_i}{f_i}$ as a reference timescale leads to non-dimensional particle-ion collision rate coefficient $H = \frac{\beta_i m_i \eta_c}{f_i a_p^3 \eta_f^2}$. Likewise, scaling of $k_B T_i$ allows the derivation of the grain-ion diffusive Knudsen number $Kn_D = \frac{\sqrt{m_i k_B T_i}\eta_c}{a_p \eta_f}$. Kn_D also parameterizes the relative importance of ballistic/vacuum ion transport to continuum/diffusive ion transport timescales: a ratio of the ballistic timescale $\frac{a_p \eta_f m_i}{\eta_c \sqrt{k_B T_i}}$ to the diffusion timescale $\left(\frac{a_p \eta_f}{\eta_c}\right)^2 \frac{f_i}{k_B T_i}$ yields Kn_D. In terms of this scaling, eq. 3a and 4a are expressed as:

$$Kn_D \to \infty: H = \sqrt{8\pi} Kn_D \ldots (5a)$$

$$Kn_D \to 0: H = 4\pi Kn_D^2 \ldots (5b)$$

At intermediate pressures, or for intermediate Kn_D, the LD methodology of Chahl and Gopalakrishnan [65] to develop a model $H = H(Kn_D, \Psi_E, S_D)$ consists of using the Langevin equation [97] to describe ion trajectories near a charged grain to infer the grain-ion collision time distribution in the presence of gas molecules. The effect of neutrals on the motion of the ion is captured implicitly through the use of a neutral drag force on the ion and a stochastic Gaussian function to mimic ion thermal motion[98]. The grain-ion collision time distribution is calculated in a periodic domain by performing a statistically significant

number (~2000) of trials as described elsewhere[57,58,65,95,96]. The non-dimensional ion flux coefficient H is parameterized as:

$$H(Kn_D, \Psi_E, S_D) = e^{\mu} H_{HS}(Kn_D) \dots (6a)$$

Here, μ is an empirical parameter that depends on Kn_D, Ψ_E, S_D:

$$\mu(Kn_D, \Psi_E, S_D) = \frac{C}{A}\left(1 + k\frac{\ln Kn_D - B}{A}\right)^{-\frac{1}{k}-1} e^{\left(-\left(1+k\frac{\ln Kn_D - B}{A}\right)^{-\frac{1}{k}}\right)}, k \neq 0 \dots (6b)$$

$H_{HS}(Kn_D)$ is an expression for H derived for the limiting case of hard-sphere interactions ($\Psi_E = 0$) between the grain and ion, described in prior work[89]:

$$H(Kn_D, \Psi_E = 0) = H_{HS}(Kn_D) = \frac{4\pi Kn_D^2 + 25.836 Kn_D^3 + \sqrt{8\pi} Kn_D (11.211 Kn_D^3)}{1 + 3.502 Kn_D + 7.211 Kn_D^2 + 11.211 Kn_D^3} \dots (6c)$$

Eq. 6 (6a, 6b and 6c) represents a model for H as a function of Kn_D, Ψ_E, S_D and converges to the limits of eq. 5a and 5b, as $Kn_D \to \infty$ and $Kn_D \to 0$, respectively. We carried out additional trajectory simulations following the methodology of Chahl and Gopalakrishnan [65] to calculate $H(Kn_D, \Psi_E, S_D)$ for $\Psi_E = 60, 100, 200, 300$; $S_D = 20, 100, \infty$ and $0.01 \leq Kn_D \leq 2000$. For the low to transition $0.01 \leq Kn_D \leq 100$, a first order time-stepping scheme[99] was used and for transition to high $10 \leq Kn_D \leq 2000$ a fourth order Runge-Kutta time stepping scheme[100] was employed to solve for the trajectories. Both numerical methods were used between $10 \leq Kn_D \leq 100$ to ensure that the choice of numerical methods had no influence on the calculated H values. The details of the numerical methods and other simulation details are described elsewhere[65,98] and we present only the simulation results and a revised fit for $\mu(Kn_D, \Psi_E, S_D)$ here. Figure S1, *SI* presents the variation of $\mu(Kn_D, \Psi_E, S_D)$ for $\Psi_E = 60, 100, 200, 300$ and for $S_D = 20, 100, \infty$. The fit constants A, B, C, k that appear in eq. 6b depend on Ψ_E, S_D and are summarized in Sec. S1, *SI* for $0.01 \leq Kn_D \leq 2000$, $0 < \Psi_E \leq 300$ and $0 < S_D < \infty$. $S_D \to \infty$ represents dilute ion concentrations or an unscreened grain interacting through the pure Coulomb potential with the ion. On the other hand, $S_D \to 0$ represents a completely screened grain typical of high ion concentrations. However, as $S_D \to 0$, at high ion concentration the average inter-ion spacing $n_i^{-1/3}$ becomes comparable with the grain-ion interaction distance $\frac{a_p \eta_f}{\eta_c}$ and it will be necessary to take into account ion-ion interactions in the Langevin framework[101]. The potential employed here $\varphi(r) = -\frac{\Psi_E}{r}\exp\left(-\frac{r}{S_D}\right)$, derived by the linearization of the Poisson-Boltzmann equation, ***neglects*** ion-ion interaction and includes only the screening of grain charge. Thus, the presented analysis is not valid at ion concentrations wherein $n_i^{-1/3} \sim \ll \frac{a_p \eta_f}{\eta_c}$, note that the ion Debye length $\lambda_D \sim n_i^{-\frac{1}{2}}$. The developed model $H_{eq.6}$ is

plotted in **Figure 1** along with the calculations of using Langevin Dynamics simulations H_{LD} for $\Psi_E = 60, 100, 200, 300$ for $S_D = 20, 100, \infty$. Also shown are the OML limit (eq. 5a) and continuum limit (eq. 5b). Figure S2, *SI* is an accompanying plot to Figure 1 that displays the % difference between $H_{eq.6}$ and H_{LD} defined as $\left(1 - \frac{H_{eq.6}}{H_{LD}}\right)\%$. It is evident from Figure S2 that eq. 6 describes H or the non-dimensional form of $\beta(p, i)$ within $\pm 10\%$ without any bias and may be considered as model for $0 < Kn_D \leq 2000,\ 0 < \Psi_E \leq 300$ and $0 < S_D < \infty$, pending experimental validation that we describe next.

Figure 1: Plots of the non-dimensional ion flux coefficient $H(Kn_D, \Psi_E, S_D)$ for $\Psi_E = 60, 100, 200, 300$ for $S_D = 20, 100, \infty$ for $0.01 \leq Kn_D \leq 2000$. In each panel, Langevin Dynamics-inferred H_{LD} is plotted using green filled circles and the predictions of the LD-based β_i model (eq. 6) is shown using the blue dashed line. Also shown are the continuum limit (eq. 5a) and free molecular limit (eq. 5b) as black dashed lines. To be read in conjunction with Figure S2 that shows the % difference between H_{LD} and $H_{eq.6}$.

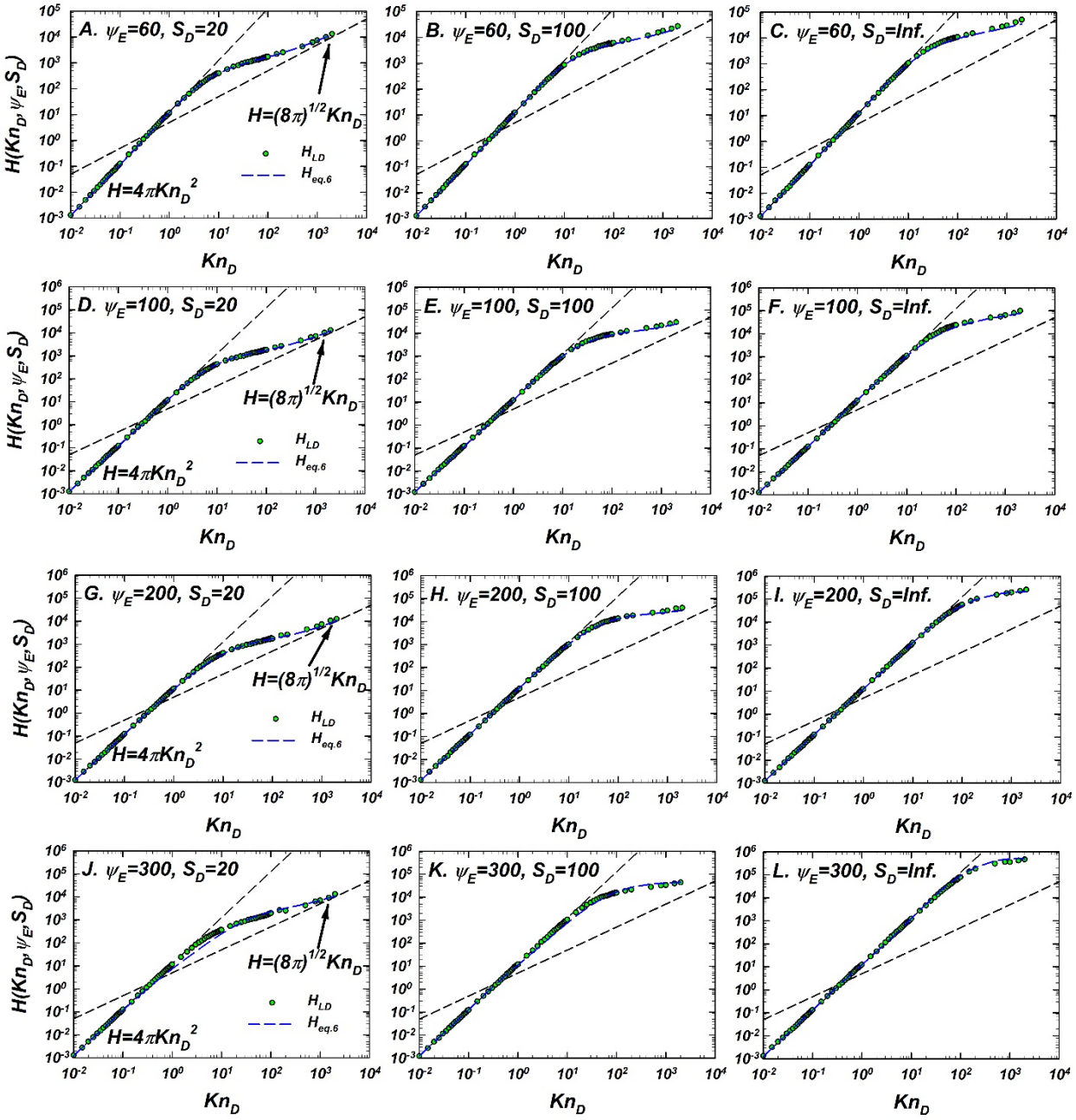

3. Experimental validation of particle-ion collision rate constant model (eq. 6) against measured grain charge in stationary plasmas

As was mentioned before, for highly charged micrometer-sized particles, the particle charge $\bar{z}_p$ may be considered to be mono-valued and calculated by equating the ion and electron currents, neglecting electron emission and assuming that positive and negative charges recombine on the surface of the particle with a probability of 1.0, if any, during the experimental runs[40,41]:

$$\beta(\bar{z}_p, i)n_i = \beta(\bar{z}_p, e)n_e \ldots (7a)$$

$\beta(\bar{z}_p, e)$, the particle-electron collision rate constant or the electron flux coefficient is calculated using collisionless OML model for repulsive interactions:

$$\beta(\bar{z}_p, e) = \left(\frac{8k_B T_e}{\pi m_e}\right)^{1/2} \pi a_p^2 \exp\left(-\frac{\bar{z}_p(-1)e^2}{4\pi\varepsilon_o a_p k_B T_e}\right) \ldots (7b)$$

The high negative charge on grains leads to a reduction of electron concentration in the plasma compared to ions leading to $\frac{n_e}{n_i} < 1$. Global charge conservation imposes the following constraint while solving eq. 7a for $\bar{z}_p$:

$$n_i = n_e + \bar{z}_p n_p \ldots (7c)$$

Thus, the grain concentration n_p also influences grain charge along with ion and electron flux transport. At low grain concentrations, the charge scavenging by grains may be neglected. Eq. 7 (7a, 7b and 7c) is solved for $\bar{z}_p$ using a simple graphical technique with the constraint that $\bar{z}_p$ is an integer. The measured grain parameters (size and number concentration), ion, electron temperature and number concentration reported[40,41] are summarized in Table S2-A and S2-B and the experimental uncertainties in the electron temperature, electron number density, particle drift velocities and electric field are summarized in Tables S2-C, *SI*. The reported parameters and uncertainties are used to estimate the nominal value and uncertainty in the experimentally measured charge z_p^{exp}.

The influence of grain concentration n_p on particle charge was experimentally determined to be minimal by Khrapak et al.[40] by measuring the particle drift velocities in the gas pressure range of 100 – 150 Pa for particle concentrations $< \sim 10^5\ cm^{-3}$. Based on this observation, the effect of particle concentration n_p was assumed to be minimal in charge calculations presented herein (i. e) $n_p = 0$ in eq. 7c. Khrapak et al.[40] also present qualitative scaling arguments to establish that their experiments were conducted in a regime wherein the particle concentrations do not appreciably perturb the plasma and

show that the ratio of particle-electron potential energy $\frac{\bar{z}_p e^2}{4\pi\varepsilon_o a_p}$ to the electron temperature $k_B T_e$ is small, allowing one to conclude that the dust particles are not a significant sink of electrons and that the plasma with dust particles has nominally the same electron concentration and temperature as the dust-free plasma. In **Figure 2**, charge on grains of radius $0.6\ \mu m$ in the pressure range of $20 - 100\ Pa$ reported by Ratynskaia et al. [41] are plotted in panel A. Experimentally measured charge with uncertainties (using two methods: force balance for a low number of particles shown as black filled circles and force balance for a high number of particles shown as blue filled squares) and computed charge (using two methods: molecular dynamics (MD) simulations shown as red filled triangles and solutions to the linear dispersion relation shown as green filled diamonds) are presented. z_p^{exp} is used to collectively denote the experimental and computationally determined charge grain datasets used for comparison with model predictions. $\bar{z}_p$, the grain charge calculated using the LD-based $\beta(\bar{z}_p, i)$ model is shown as a black solid line in panel A. Upper and lower bounds of the prediction, taking into account the measurement uncertainty in electron temperature and number concentration are shown as black dashed lines. The equations used to estimate the prediction bands is provided in Sec. S2-C, *SI*. The difference between predictions and experiment are quantified as $\frac{\bar{z}_p}{z_p^{exp}}$ (panel B) and with reference lines at $0.7, 0.8, 1.2, 1.3$ to show identify data points with $\pm 30\%$ and $\pm 20\%$ agreement with validation datasets[40,41]. **Figure 2-A** clearly demonstrates that the LD-based $\beta(\bar{z}_p, i)$ model (eq. 4) reproduces the trend observed in the experiment and **Figure 2-B** shows excellent agreement within $\pm 20\%$. Panels (C, D) , (E, F) and (G, H) show comparisons of electric charge for grains of radius $0.6\ \mu m, 1\ \mu m$, and $1.3\ \mu m$, respectively, reported by Khrapak et al. [40] and corresponding predictions $(\bar{z}_p)$ as a function of gas pressure in the range of $20 - 150\ Pa$. Similar to panels (A, B), the LD-based β_i model's charge predictions agree very well with z_p^{exp} for all the three grain sizes as shown in panels C, E, G. Panels D, F, H illustrate this as well, showing the ratio of the predicted grain charge $\bar{z}_p$ to z_p^{exp}: nominally, the LD-based $\beta(\bar{z}_p, i)$ model predicts grain charge to within $\pm 35\%$ in dilute dusty plasmas (with grain concentration $n_p \leq 10^5 cm^{-3}$ and ion concentration $n_i \leq 10^8\ cm^{-3}$) for pressures up to $150\ Pa$. It can be clearly observed that most of the data (measured and computed) fall in the range between the upper and lower prediction band (the black dashed lines in panels A, B, C, D above and below the model prediction curve). There is some deviation of experimental measurements from the theoretical model at lower pressures $< 50\ Pa$, while at higher pressures up to $\sim 150\ Pa$ there is excellent agreement without appreciable bias. The less than satisfactory agreement below $50\ Pa$ is a part of systematically lower predictions in rarefied conditions by the LD-based model as well as other models[40,70]. This indicates that additional mechanisms of electron transport may be active at low pressures and requires further examination in future theoretical work. The range of non-dimensional

parameters probed by the experimental data is summarized in Table S2-D, *SI* as $76 < \Psi_E < 137, 42 < S_D < 189, 9 < Kn_D < 354$.

Figure 2: (A, B) Plot of the magnitude of particle charge z_p^{LD} as a function of gas pressure p_g showing experimental data z_p^{exp} reported by Ratynskaia et al. [41] for particle radius $a_p = 0.6\ \mu m$ as discrete data points ("exp" denotes experimentally obtained grain charge: black filled circles for a low number force balance method, blue filled squares for a high number force balance method along with reported uncertainties; "sim" denotes computated grain charge: red filled triangles for MD simulations, green filled diamonds for solutions to a dispersion relation). Particle charge z_p^{LD} calculated by solving eq. 7 with the LD-based β_i model (eq. 6) is shown using the black solid line. Black dashed lines are used to denote the upper and lower prediction bands of the model calculation. **B.** Plot of $\frac{z_p^{LD}}{z_p^{exp}}$ with reference lines at $0.7, 0.8. 1.2, 1.3$ (black dashed lines) to show $\pm 20\%, \pm 30\%$ difference between the validation data and model predictions. **(C, D)** Plot of z_p^{LD} as a function of p_g showing z_p^{exp} data reported by Khrapak et al. [40] for $a_p = 0.6\ \mu m$ and the corresponding $\frac{z_p^{LD}}{z_p^{exp}}$. **(E, F)** $z_p^{LD}(p_g)$ along with z_p^{exp} data reported by Khrapak et al. [40] for $a_p = 1.0\ \mu m$ and the corresponding $\frac{z_p^{LD}}{z_p^{exp}}$. **(G, H)** $z_p^{LD}(p_g)$ along with z_p^{exp} data reported by Khrapak et al. [40] for $a_p = 1.3\ \mu m$ and the corresponding $\frac{z_p^{LD}}{z_p^{exp}}$.

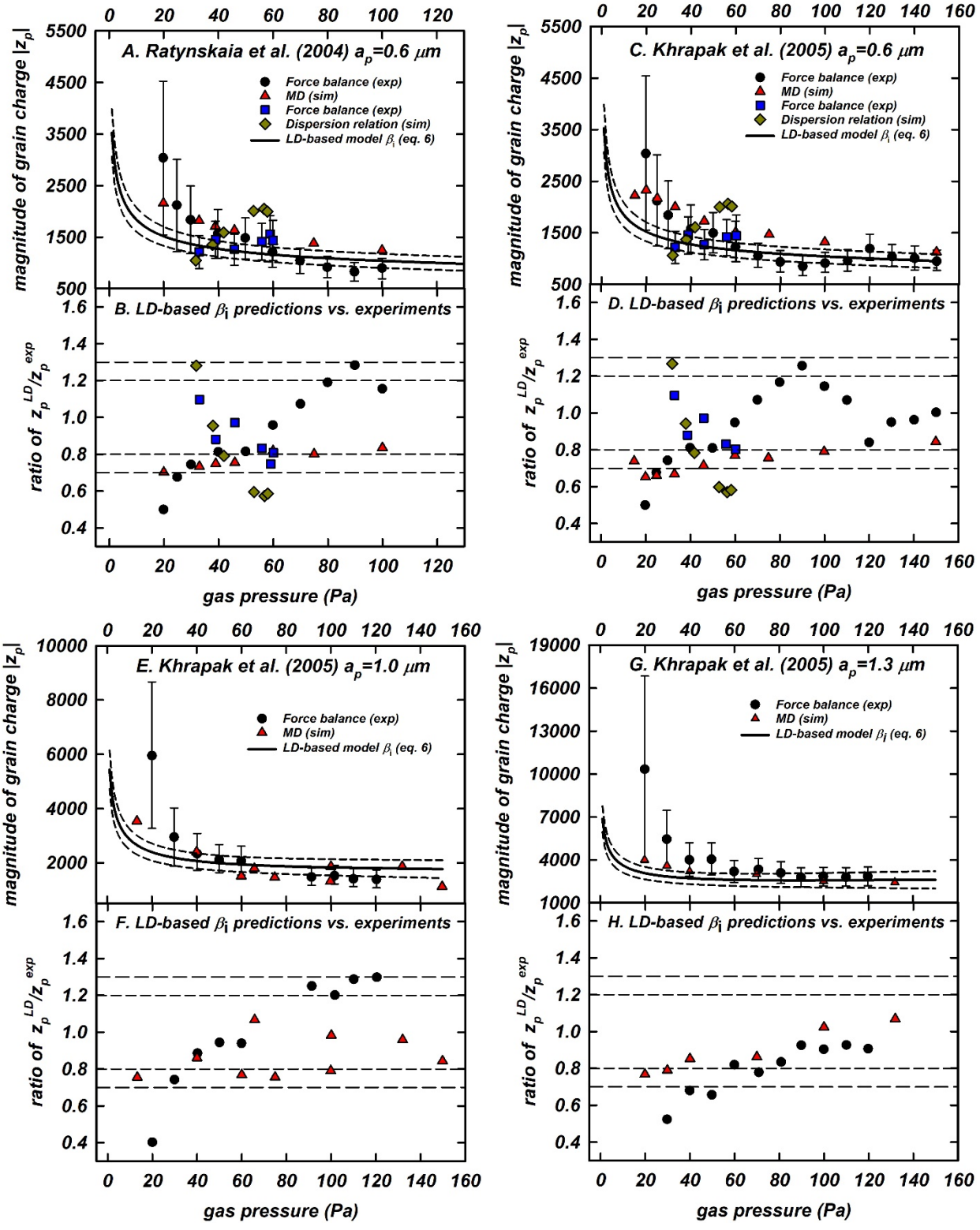
A. Ratynskaia et al. (2004) a_p=0.6 μm
C. Khrapak et al. (2005) a_p=0.6 μm
E. Khrapak et al. (2005) a_p=1.0 μm
G. Khrapak et al. (2005) a_p=1.3 μm
Force balance (exp)
MD (sim)
Dispersion relation (sim)
LD-based model β_i (eq. 6)
magnitude of grain charge $|z_p|$
B. LD-based β_i predictions vs. experiments
D. LD-based β_i predictions vs. experiments
F. LD-based β_i predictions vs. experiments
H. LD-based β_i predictions vs. experiments
ratio of z_p^{LD}/z_p^{exp}
gas pressure (Pa)

4. $\beta(p,i)$ model for particle at low $(|z_p|\sim 0)$ and high $(-z_p \gg 0)$ charge levels

Before we describe our modeling of the particle charge distribution in the plasma afterglow by solving eq. 2 and the assumptions therein to obtain the particle charge distribution, we briefly summarize the $\beta(p,i)$ model derived by Li et al. [57] that accounts for both Coulomb and image potential interactions at finite gas pressures. Similar to Ψ_E, the potential energy associated with electrostatic image or polarization forces on the ion is parameterized by a dimensionless ratio: $\Psi_I = \frac{\varepsilon_r - 1}{\varepsilon_r + 1} \frac{z_i^2 e^2}{4\pi\varepsilon_0 a_p k_B T_i}$. By definition $\Psi_I > 0$ and the ratio $\frac{\Psi_I}{|\Psi_E|} = \frac{z_i}{|z_p|}$ captures the relative importance of the image potential to the coulomb potential on particle-ion collisions. It is readily seen that the image potential is most important for low charge levels on particles $(|z_p| \to 0)$ and may be ignored otherwise $(-z_p \gg 0)$. Li et al. [57] provide an extension of eq. 6b by modifying the scaling analysis of Section II-A to include $\frac{\Psi_I}{|\Psi_E|}$ while assuming $S_D \to \infty$ (dilute ion concentrations) and provide succinct regressions for the continuum and free molecular enhancement factors $\eta_c(\Psi_E, \Psi_I), \eta_f(\Psi_E, \Psi_I)$ in the range $-60 \le \Psi_E \le 60, 0 \le \frac{\Psi_I}{|\Psi_E|} \le 1$ therein[57]. Section S3, *SI* presents A, B, C, k values applicable for $-60 \le \Psi_E \le 60, 0 \le \frac{\Psi_I}{|\Psi_E|} \le 1$ to describe aerosol particle charging in the $0 < Kn_D \le 2000$ mass transfer regime using eq. 6a. This parameterization (eq. 6) has been tested against both experimentally measured unipolar and bipolar charge distributions for spherical aerosol particles and in a later report, Li and Gopalakrishnan [56] generalize eq. 6 to particles of arbitrary shapes as well for the same range of Ψ_E, Ψ_I, Kn_D along with comparison to bipolar diffusion charging data. Thus, to calculate $\beta(p,i)$, the extended model of Chahl and Gopalakrishnan [65] described in Section II-A (A, B, C, k regressions summarized in Section S1, *SI*) is used for $60 < \Psi_E \le 300, 0 < S_D < \infty, 0 < Kn_D \le 2000$ when the magnitude of particle charge is much higher than zero $(-z_p \gg 0, \Psi_E > 60)$. For low particle charge levels $(|z_p| \to 0, \Psi_E \le 60)$, the $\beta(p,i)$ developed by Li et al. [57] (A, B, C, k regressions summarized in Section S3, *SI*) are used for $-60 \le \Psi_E \le 60,\ S_D \to \infty, 0 \le \frac{\Psi_I}{|\Psi_E|} \le 1, 0 < Kn_D \le 2000$.

5. Estimation of particle charge distribution in the afterglow with spatially varying ion and electron concentrations

Particle charging in the afterglow is system- as well as process-specific and is modeled here taking into account the dimensions of the flow reactor, gas flow and plasma conditions employed while measuring the particle charge distribution $f_p(d_p)$ as a function of particle diameter d_p.The plasma reactor used by Sharma et al. [23] is a cylindrical tube of inner diameter $2R = 2\ mm$ with an active plasma region of length 2 cm and an afterglow that was nominally considered to be $L = 2\ cm$. Argon gas flow rate $Q = 1\ SLPM$ was used and is assumed here to be of uniform velocity $\frac{Q}{\pi R^2}$ through the reactor. AC and RF power driven non-thermal plasmas were investigated experimentally[23] but we choose to model only the dataset corresponding to an RF power of 2.5 W. The LD-based $\beta(p,i)$ model is dependent on the concentration and temperature of the ions but does not directly depend on the type of plasma excitation (RF/AC) used for ionization of the background gas. The electron concentration n_e estimated by the authors and measured electron temperature $k_B T_e$ vary no more than a factor of 2 over the 2.5 – 45 W RF power range absorbed by the plasma in the experiments. Hence, for simplicity, we take $n_e = 0.5 \times 10^{15}\ m^{-3}, k_B T_e = 0.51\ eV, T_i = T_g = 300\ K$ in the plasma. The estimate of n_e is based on the remarks of Dhawan et al. [26], a follow-up study to the observations reported by Sharma et al. [23], that a choice of $2.5 \times 10^{15}\ m^{-3}$ leads to reasonable agreement between the characteristic charging time analysis and their experimental results. Although our choice of electron concentration is 5 times smaller, we also explore the variation in the predicted particle charges with variability in electron concentration. The ion and electron concentration that exists at the end of the plasma region (the start of the afterglow) influences the charge distribution strongly and the influence of the same on the charge distributions will be discussed shortly along with comparison of predictions to measurements. The gas temperature is assumed to be $T_g = 300\ K$ although Sharma et al. [23] and prior work[102] suggests that there is significant heating of the gas by the plasma species. While the axial temperature profile or downstream temperature was not measured presumably, because of ~1 mm tube diameter, modeling the same is considered beyond the scope of this work because the collisional heating of the gas by plasma generated species in not fully understood theoretically yet. The ion diffusion constant D_i is calculated based on the reduced mobility $\mu^r_{Ar^+} = 1.4\ m^2 s^{-1} V^{-1}$of Ar^+ reported by McAfee et al. [103] at $p_g = 760\ torr, T_g = 300\ K$ using the Stokes-Einstein equation: $D_i = \frac{k_B T_i}{e} \mu^r_{Ar^+} \left(\frac{760}{p_g}\right)\left(\frac{T_g}{273.16}\right)$. The electron diffusion constant $D_e = 0.0681\ m^2 s^{-1} V^{-1}$ reported in a recent study[10] at 300 K and atmospheric pressure in Argon was used. The particle diffusion constant D_p is also calculated using the Stokes-Einstein equation with the particle friction factor f_p evaluated as $f_p = \frac{6\pi\mu_g a_p}{1+\alpha_1\left(\alpha_2 + Kn \cdot e^{-\frac{\alpha_3}{Kn}}\right)}$ and $D_p = \frac{k_B T_g}{f_p}$. Here, corresponding to air[104]: $\alpha_1 = 1.257, \alpha_2 =$

$0.4, \alpha_3 = 1.1$ (not argon, because values for argon are not available and that the coefficients only weakly vary with gas) and $\mu_g = \left(2.25 \times 10^{-5}\ Pa.s\right)\left(\frac{296.15\ K+141.4\ K}{T(K)+141.4\ K}\right)\left(\frac{T(K)}{141.4\ K}\right)^{\frac{3}{2}}$ is the argon gas viscosity for the experimental conditions. D_p is used for all particles regardless of their charge state p. $Kn = \frac{\lambda_g}{a_p}$ is the particle momentum Knudsen number based on the gas mean free path $\lambda_g = \frac{\mu_g}{0.499\rho_g\bar{c}}$; $\rho_g = \frac{p_g}{RT_g}$ is the gas density, $\bar{c} = \left(\frac{8k_BT_g}{\pi m_g}\right)^{\frac{1}{2}}$ is the gas molecule mean thermal speed and m_g is the mass of a gas molecule. Owing to the species residence time in the plasma $t_r = \frac{\pi R^2 L}{Q} \sim 4 \times 10^{-3}\ s$ being larger than the particle-ion collision time $\tau = \frac{1}{\beta(0,i)n_i} \sim 2 \times 10^{-4}\ s$ for 100 nm particle colliding with an ion at $n_i \sim 0.5 \times 10^{15}\ m^{-3}$ and based on $\beta(p = 0, i) \sim 10^{-11}\ m^3 s^{-1}$ atmospheric pressure and 300 K, it is assumed that particle charge distribution attains a steady state during flow through the plasma and the afterglow and the species transport equations for the ion, electron and particles carrying p charges (eq. 2) are solved in 2-D axisymmetric cylindrical coordinates (r, z) using COMSOL® Multiphysics commercial software with these choices for rate constants:

1. As discussed later, ambipolar diffusion is neglected and diffusion is assumed to be the dominant loss mechanism for both ions and electrons, the ion-electron recombination rate in the afterglow is neglected from both eq. 2a and 2b for simplicity: $R_{ie} = 0$.
2. $\beta(p, i) = H\frac{f_i a_p^3 \eta_f^2}{m_i \eta_c}$ is calculated using eq. 6 with the parameter μ given by Section S1, *SI* for $60 < \Psi_E \leq 300$ and given by Section S3, *SI* for $-60 \leq \Psi_E \leq 60, 0 \leq \frac{\Psi_I}{|\Psi_E|} \leq 1$ for $0 < Kn_D \leq 2000$. As mentioned before, $\Psi_E = -\frac{p(+1)e^2}{4\pi\varepsilon_0 a_p k_B T_i}$; $\Psi_I = \frac{\varepsilon_r - 1}{\varepsilon_r + 1}\frac{(+1)^2 e^2}{4\pi\varepsilon_0 a_p k_B T_i}$; $Kn_D = \frac{\sqrt{m_i k_B T_i}}{f_i a_p}\frac{\eta_c}{\eta_f}$; $\eta_f(\Psi_E, S_D), \eta_c(\Psi_E, S_D)$ are calculated using eq. 3b and eq. 4b, respectively, for $60 < \Psi_E \leq 300$ and $\eta_f(\Psi_E, \Psi_I), \eta_c(\Psi_E, \Psi_I)$ are calculated using the regressions presented by Li et al. [57] for $-60 \leq \Psi_E \leq 60$. Finally, $d_p \sim 15 - 80\ nm\ MgSO_4$ particles are considered to be perfectly conducting $(\varepsilon_r \to \infty)$ in our analysis.
3. $\beta(p, e)$ is calculated using the OML model (eq. 3) including Coulomb potential only:

$$\beta(p, e) = \left(\frac{8k_BT_e}{\pi m_e}\right)^{1/2} \pi a_p^2 \eta_f(\Psi_E^e) \ldots (8a)$$

$$\eta_f(\Psi_E^e) = \begin{cases} 1 + \Psi_E^e, \Psi_E^e \geq 0 \\ \exp(\Psi_E^e), \Psi_E^e \leq 0 \end{cases} \ldots (8b)$$

$$\Psi_E^e = -\frac{p(-1)e^2}{4\pi\varepsilon_0 a_p k_B T_e} \ldots (8c)$$

Eq. 2 is solved in an axisymmetric cylindrical domain $r \epsilon [0, R = 1\ mm], z \epsilon [0, L = 2\ cm]$ with zero concentration at the tube wall $(r = R, z)$ and zero flux at the outlet $(r, z = L)$:

$$r = 0, z: \frac{\partial n_i}{\partial r} = \frac{\partial n_e}{\partial r} = \frac{\partial n_p}{\partial r} = 0 \ldots (9a)$$

$$r = R, z: n_i = n_i = n_p = 0 \ldots (9b)$$

$$r, z = L: -D_i \frac{\partial n_i}{\partial z} = -D_e \frac{\partial n_i}{\partial z} = -D_p \frac{\partial n_p}{\partial z} = 0 \ldots (9c)$$

At the inlet $(r, z = 0)$, the ion and electron concentrations are taken to be equal to the magnitudes in the plasma region upstream $(z < 0)$:

$$r, z = 0: n_i = n_e = N_{c0} \ldots (9d)$$

$$r, z = 0: n_p = N_{p0} \ldots (9e)$$

N_{c0} chosen to be $0.5 \times 10^{15}\ m^{-3}$ and this choice is discussed shortly. The concentration of particles carrying p charges n_p is determined from the $MgSO_4$ aerosol particle size distribution, reported by Sharma et al. [23] when their aerosol generator with the plasma OFF and is taken to be the size and number concentration entering the plasma region during the charging measurements. Although a wide size distribution enters the plasma reactor, we consider the charging of particles to be independent of the presence of particles of other sizes. Thus, in our modeling, we assume that particles of fixed diameter are exposed to ions and electrons of the same concentration although in reality, a wide size range of particles are simultaneously flowing and interacting with ions. This assumption has implications for the available ion and electron concentration to each particle and will be also discussed along with our choice of N_{c0}. Also neglected is the ambipolar diffusive flux $\left(-z_{i(e)} e \mu_{i(e)} \nabla \varphi\right)$ of the ions and electrons due to the net positive space charge environment that exists in the afterglow region due to higher thermal diffusivity of the electrons than the ions. The resulting electric field $-\nabla \varphi$, governed by a Poisson equation $-\nabla \cdot \nabla \varphi = \frac{e}{\varepsilon_0}(n_i - n_e)$, nominally drives the ions towards the walls and electrons towards the center, leading to faster depletion of the former along the axis of the flow reactor (than predicted by eq. 2a) and slower axial drop of the electron concentration (than calculated using eq. 2b). The longer persistence of the electrons and shorter life of ions than expected, will most likely shift the predicted charge distributions to more negative states than reported here. Since it was seen that the charge distribution attains an axially independent value $\left(\frac{\partial f_p}{\partial z} \approx 0\right)$ within a small fraction from the beginning of the afterglow, this effect is assumed to be small enough not to quantitatively influence the predicted charge fractions to avoid numerical difficulties in solving eq. 2 along with the Poisson equation for electric potential profile in the afterglow. The number concentration of particles entering the afterglow is taken to the same as the concentration entering the plasma region (neglecting diffusional losses) and is estimated as $N_{p0}(d_p) =$

$\frac{dc}{d\log d_p}\Delta\log d_p$. $\frac{dc}{d\log d_p}$ is the particle size distribution function measured by Sharma et al.[23] using aerosol electrical mobility analysis; c is the number concentration of particles, d_p is used to denote particle diameter and $\Delta\log d_p$ corresponds to the resolution of the reported $\frac{dc}{d\log d_p}$ data. The estimated particle concentration N_{p0}, after being exposed to the plasma region $(z<0)$, attains a steady state (negative) charge $\bar{z}_p(<0)$ that is calculated by solving eq. 1 with $\beta(p,i)$ given by eq. 6 and with regression parameters in Section S1, *SI* and $\beta(p,e)$ given by eq. 9. **Figure 3-A** presents N_{p0} (m^{-3}) used in eq. 9e and $\bar{z}_p$ that is for each particle size considered as a function of the particle diameter d_p (nm); predictions for $n_e=0.5\times10^{15}\,m^{-3}, k_BT_e=0.51\,eV, T_g=300\,K$ alone are presented as analogous predictions for $n_e=1\times10^{15}\,m^{-3}$ and $n_e=2.5\times10^{15}\,m^{-3}$ do not differ significantly. For each particle, depending on the charge $\bar{z}_p(<0)$ with which it enters the afterglow, p is varied between $\bar{z}_p-2$ to $+4$ to capture the evolution of the charge distribution as a function of axial position z; eq. 2c represents $\left(5+\left|\bar{z}_p-2\right|\right)$ equations to track the concentration n_p of particles carrying p charges. At the outlet of the computational domain $(r,z=R)$, the particle charge distribution f_p is calculated for comparison with corresponding measurements[23] as:

$$f_p=\frac{\langle n_p(r,z=R)\rangle_r}{\sum_{p=\bar{z}_p-2}^{+4}\langle n_p(r,z=R)\rangle_r}\ldots(10)$$

$\langle\cdot\rangle_r$ denotes averaging over the cross section at a particular z. f_p calculated using eq. 10 is compared with corresponding experimental data for $15-80\,nm\;MgSO_4$ particles. The fraction of charged particles $(1-f_0)$ as a function of d_p, obtained experimentally for RF powers of 2.5 W and 18.9 W is plotted in **Figure 3-B** along with corresponding model predictions for $n_e=0.5\times10^{15}\,m^{-3}, 1\times10^{15}\,m^{-3}, 2.5\times10^{15}\,m^{-3}$. Firstly, it is seen that the experimental data for the two RF powers do not significantly differ from each other. Further, the predictions are seen to be sensitive to n_e and lead to best agreement with data for $0.5\times10^{15}\,m^{-3}$. The % difference calculated as $\left(1-\frac{(1-f_0)_{n_e=0.5\times10^{15}\,m^{-3}}}{(1-f_0)_{RF}}\right)\%$ between experimental data and model predictions for $n_e=0.5\times10^{15}\,m^{-3}$ shown in Fig. 3-C is within $\pm20\%$ nominally. As mentioned before, the ion/electron concentration entering the afterglow region is strongly influenced by the particle charging processes in the plasma region upstream. The volumetric loss rate of ions to particles may be estimated as $R_{pi}=\int_{d_p=0}^{d_p=\infty}\sum_{p=-\infty}^{p=+\infty}\beta(p,d_p,i)f(p,d_p)\frac{dN}{d\log d_p}d\log d_p$, where $f(p,d_p)$ is the fraction of particles of charge state p and size d_p and $\beta(p,d_p,i)$ is the corresponding particle-ion collision rate constant. Since knowing $f(p,d_p)$ apriori is, by-definition, not possible, the ion concentration at the end of the plasma region, approximated as $n_i-R_{pi}\tau$, cannot be estimated by modeling alone; $\tau=\frac{\pi R^2L}{Q}$ is the residence time in the plasma

region. Likewise, the electron volumetric loss rate, $R_{pe} = \int_{d_p=0}^{d_p=\infty} \sum_{p=-\infty}^{p=+\infty} \beta(p, d_p, e) f(p, d_p) \frac{dN}{d \log d_p} d \log d_p$, also determines the nominal electron concentration at the beginning of the afterglow region $(n_e - R_{pe}\tau)$. It is necessary that the ion and concentrations be known from measurement towards the end of the plasma region, a challenging measurement to carry out, considering the ~1 mm radius of the cylindrical tube used for the plasma reactor. Another degree of freedom in the model calculations is the gas temperature T_g that also strongly affects the model predictions. Since it is known that the gas is warmed by the plasma, an average measure of the axial temperature profile, also limited by the minute dimensions of the plasma reactor, is desirable to be used in modeling of particle charging in plasma afterglows. Although the experimental data is reported for each RF power employed in the range of $2.5 - 45\ W$, our predictions do not depend on power and are compared the data set based on RF power of 2.5 W, that themselves vary only weakly with applied power[23]. We recognize that, like electron concentration, the electron temperature and gas temperature can also have a possible range of variation. Even though this uncertainty band may not be accurately estimated, we nevertheless attempt to understand the effect of spread in electron temperature and gas temperature by carrying out additional simulations, presented in **Figure 5** and **Figure 6**, respectively. The effect of electron temperature is investigated by varying $k_B T_e = 0.25, 0.51, 1\ eV$ while holding $n_e = 0.5 \times 10^{15}\ m^{-3}, T_g = 300\ K$. **Figure 5-A** depicts the particle charge $\bar{z}_p$ exiting the plasma region. As expected, there is a significant (monotonous) dependence on electron temperature in the $0.25 - 1\ eV$ range. Interestingly, as shown in **Figure 5-B**, the particle charge fractions are nearly independent of the electron temperature in the afterglow region and produce excellent agreement with the experimental data (for both RF powers 2.5 W and 18.9 W). The effect of gas temperature is similarly shown in **Figure 6-A** (particle charge for 300 K, with 450 K and 600 K leading to similar particle charge exiting the plasma) and **Figure 6-B**. **Figure 6-B** shows that predictions increasingly deviate from experimental data with increasing gas temperature. Although, we did not model it explicitly, the gas temperature in the afterglow is expected to be >300 K but <450 K (the gas temperature entering the plasma region in the experiment is estimated to be ~423 K). Thus, while excellent agreement is obtained for 300 K, a reasonable agreement is also seen for 450 K. This emphasizes the need to measure the axial gas temperature profile in the afterglow region in order to model particle charging more accurately. As shown in **Figure 6-A** and **Figure 6-B** for $d_p = 15\ nm$ and $d_p = 45\ nm$, respectively, charge fractions measured at various powers only slightly and are taken to be nominally the same as that measured at any power in that range; we chose the dataset corresponding to 2.5 W. Our f_p predictions are compared with experimental data in **Figure 6-C** and **Figure 6-D** for $d_p = 15\ nm$ and $d_p = 45\ nm$, respectively. In these comparisons, the ion and electron concentrations used in the boundary condition (eq. 9d) are varied $n_e = (0.5, 1, 2.5) \times 10^{15}\ m^{-3}$ to show the sensitivity

of ion/electron concentration at the beginning of the afterglow on the steady-state charge distributions attained further downstream. In the experimental runs, it is seen that most of the particles attain a neutral charge distribution with most of the particles having $-1, 0$ or $+1$ charges. In terms of measuring their number concentration using a condensation particle counter with an aerosol differential mobility analyzer upstream to select particles based on their charge to drag ratios, as was employed by Sharma et al. [23], these charge fractions are measured with lower counting uncertainty compared to charge states of $\pm 2, \pm 3,$ .... Thus, our model predictions are able to reproduce the most reliably measured moments of the charge distribution accurately with $n_e = 5 \times 10^{14}\ m^{-3}$. It is also seen that the charge distribution is shifted further to positive mean charge as n_e is varied to $1 \times 10^{15}\ m^{-3}$ and $2.5 \times 10^{15}\ m^{-3}$. This shows that the particle charge distribution can also be controlled by varying n_e in a non-thermal plasma and the need to measure n_e in the presence and absence of particles in future experiments order to enable modeling of particle charge using the particle-ion collision rate constant model advanced here. Based on the number concentrations reported in **Figure 3-A** and nominal $\beta(p = 0, i)$, it can be estimated that $\beta\left(p = 0, d_p, i\right) \frac{dN}{d \log d_p} d \log d_p$ is at least a factor 10^4 higher for larger for $100\ nm$ than $10\ nm$ particles. Thus, the ion/electron concentration reduction due to collisional charging is a significant sink term for $\sim 80\ nm$ particles than $< 20\ nm$ nanoparticles. The experimental design of Sharma et al. [23] flew a polydisperse population of $MgSO_4$ particles into the non-thermal plasma before charge fractions were measured. It is recommended that using a mobility classifier upstream of the non-thermal plasma to size-select or use monodisperse particles for experimentation will allow the modeling of ion loss to particles of a fixed size and improve the accuracy of using eq. 2. Currently, R_{pi} and R_{pe} are not included in eq. 2a and 2b and are likely to be much higher than $\sum_{p=-\infty}^{p=+\infty} \beta(p, i) n_p n_i$ and $\sum_{p=-\infty}^{p=+\infty} \beta(p, e) n_p n_e$ included. In fact, based on our estimates, it is possible that $\frac{\sum_{p=-\infty}^{p=+\infty} \beta(p,i) n_p n_i}{R_{pi}} < 0.1$. Thus, the reduced ion and electron concentrations at the exit of the plasma producing good agreement with measured charge fractions is not entirely fortuitous. A properly measured axial ion and electron concentration profile will allow the prediction and design of plasma process conditions to tune the particle charge distribution in the afterglow[25,26]. Another assumption in the modeling is that the charging reactions attain a steady state within the afterglow (based on the residence times of the particles in the plasma). While this assumption certainly becomes better for particles > 100 nm, sub-80 nm particles considered here have characteristic particle-ion collision times (the slower among particle-ion and particle-electron collisions) and for ~10 nm particles, it is possible that the particles took much longer than the 2 cm region nominally taken to be the afterglow (in our modeling as well as in the experiments[23,26]). Inclusion of an unsteady term in eq. 2 thus becomes necessary for small particles and must be explored in future work. Finally, yet another challenge in modeling particle

charging in afterglows, for $\sim 5\ \mu m$ sized particles in an inductively coupled non-thermal plasma at $\sim 90\ Pa$ reported by van Minderhout et al. [24], is that exiting the plasma region the particle negative charge is $-z_p \sim 4000 e^-$. Tracking ~4000 equations for each charge state in eq. 2c is practically difficult requiring a semi-continuous sectional representation of charge state that transitions from continuous for highly charged states $\left(-z_p \gg 0\right)$ to discrete $\left(\left|z_p\right| \sim 0\right)$ for low charge states. Qualitatively, the discussion presented here applies to the measurements of van Minderhout et al. [24] as well and needs to be modeled in future work.

Figure 3: A. Particle number concentration estimated from size distribution reported by Sharma et al. [23] (grey filled squares) used in eq. 9e and the particle charge calculated from eq. 8 as the state of charge of particles exiting the plasma and entering the afterglow calculations (eq. 2) as a function of particle diameter d_p for $n_e = 5 \times 10^{14}\ m^{-3}$. Similar calculations for $n_e = 1 \times 10^{15}\ m^{-3}$ and $n_e = 2.5 \times 10^{15}\ m^{-3}$ yield particle charge values that are nearly identical and so, are not displayed. **B.** Fraction of charged particles $(1 - f_0)$ as a function of d_p, obtained experimentally for RF powers of 2.5 W and 18.9 W and model predictions (eq. 2) for $n_e = 5 \times 10^{14}\ m^{-3}, 1 \times 10^{15}\ m^{-3}, 2.5 \times 10^{15}\ m^{-3}$. **C.** % difference calculated as $\left(1 - \frac{(1-f_0)_{n_e=5\times10^{14}\ m^{-3}}}{(1-f_0)_{RF}}\right)\%$ between experimental data (RF power 2.5 W and 18.9 W) and model predictions for $n_e = 5 \times 10^{14}\ m^{-3}$

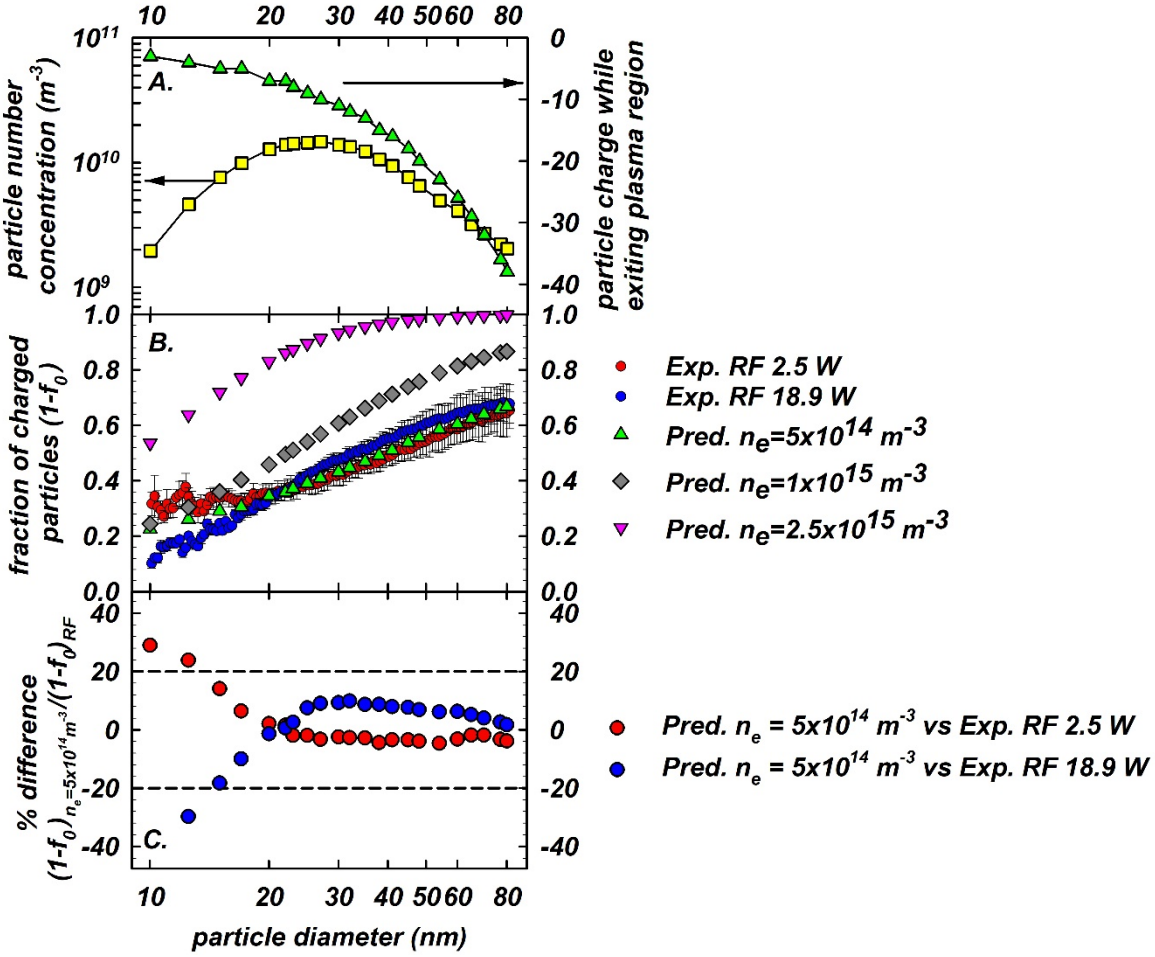

Figure 4: A. Particle charge calculated from eq. 8 as the state of charge of particles exiting the plasma and entering the afterglow calculations (eq. 2) as a function of particle diameter d_p for electron temperatures of $0.25,0.51,1\ eV$. **B.** Fraction of charged particles $(1-f_0)$ as a function of d_p, obtained experimentally for RF powers of 2.5 W and 18.9 W and model predictions (eq. 2) for $k_BT_e = 0.25, 0.51, 1\ eV$.

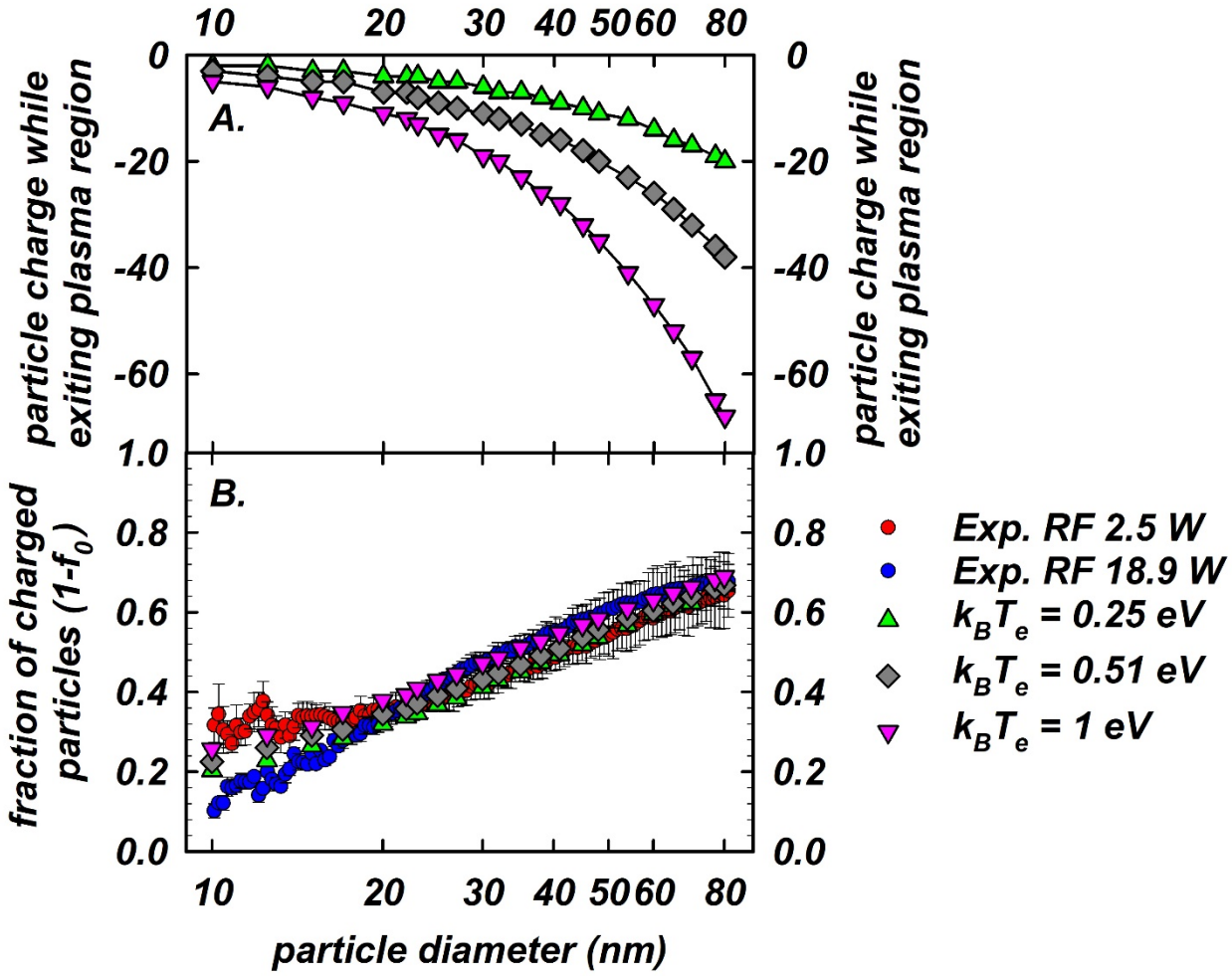

Figure 5: A. Particle charge calculated from eq. 8 as the state of charge of particles exiting the plasma and entering the afterglow calculations (eq. 2) as a function of particle diameter d_p for gas temperature of $300\ K$. Similar calculations for $450\ K$ and $600\ K$ yield particle charge values that are nearly identical and so, are not displayed. **B.** Fraction of charged particles $(1 - f_0)$ as a function of d_p, obtained experimentally for RF powers of 2.5 W and 18.9 W and model predictions (eq. 2) for $T_g = 300, 450, 600\ K$.

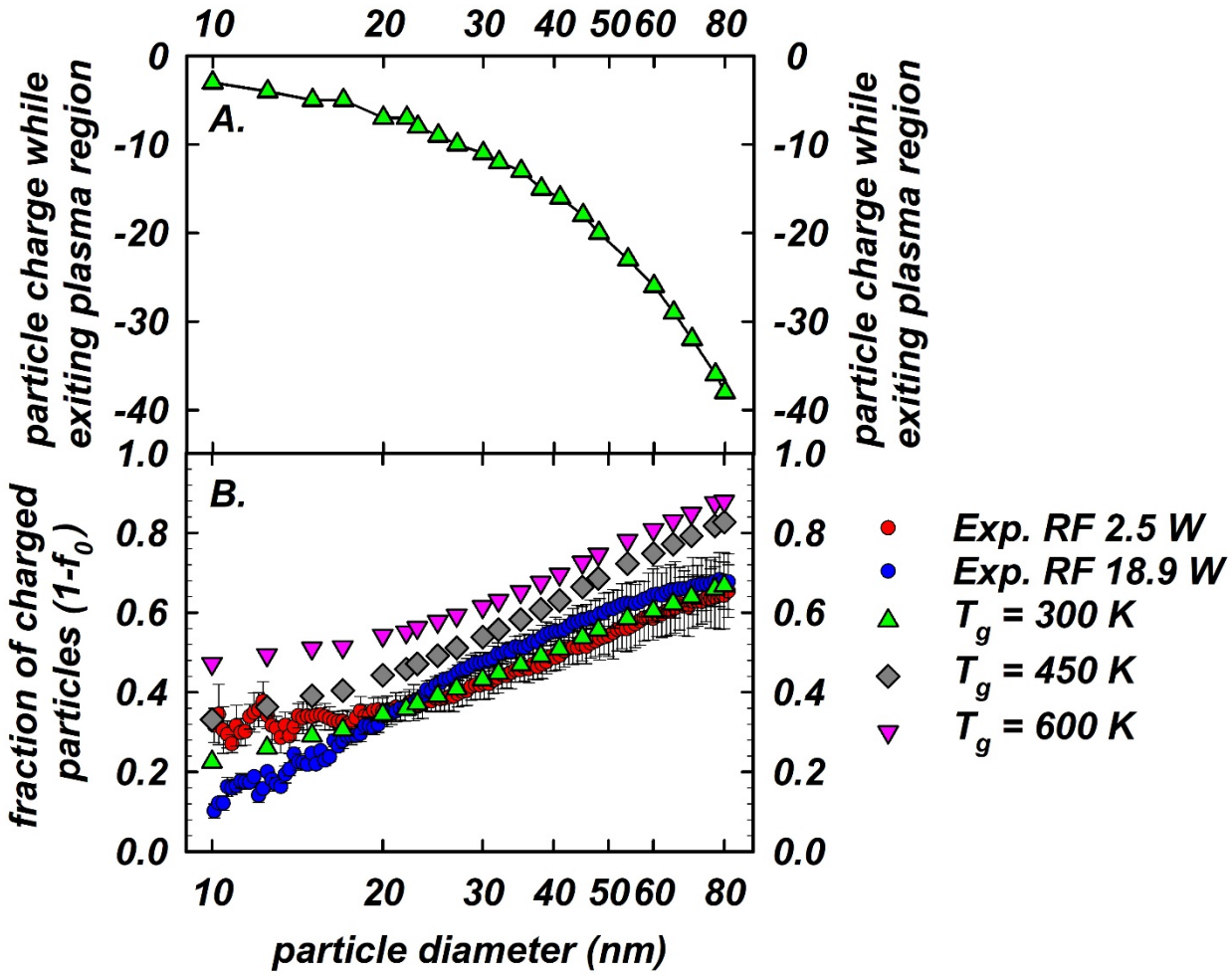

Figure 6: (A, B) Experimentally measured charge fractions reported by Sharma et al. [23] for 15 nm and 45 nm $MgSO_4$ aerosol particles exposed to non-thermal plasmas driven by RF powers 2.5 – 25 W. It is seen that the charge distribution is nominally insensitive to RF power for the presented data. **(C, D)** Comparison between experimental data and predictions for 15 nm and 45 nm $MgSO_4$ aerosol particles corresponding to an RF power of 2.5 W only and three sets of model predictions (eq. 2) with $n_e = 5 \times 10^{14}\, m^{-3}, 1 \times 10^{15}, n_e = 2.5 \times 10^{15}\, m^{-3}$. It is seen that the model accurately reproduces charge states of $-1, 0, +1$ well and that the choice of nominal ion/electron concentration significantly influences the particle charge distribution.

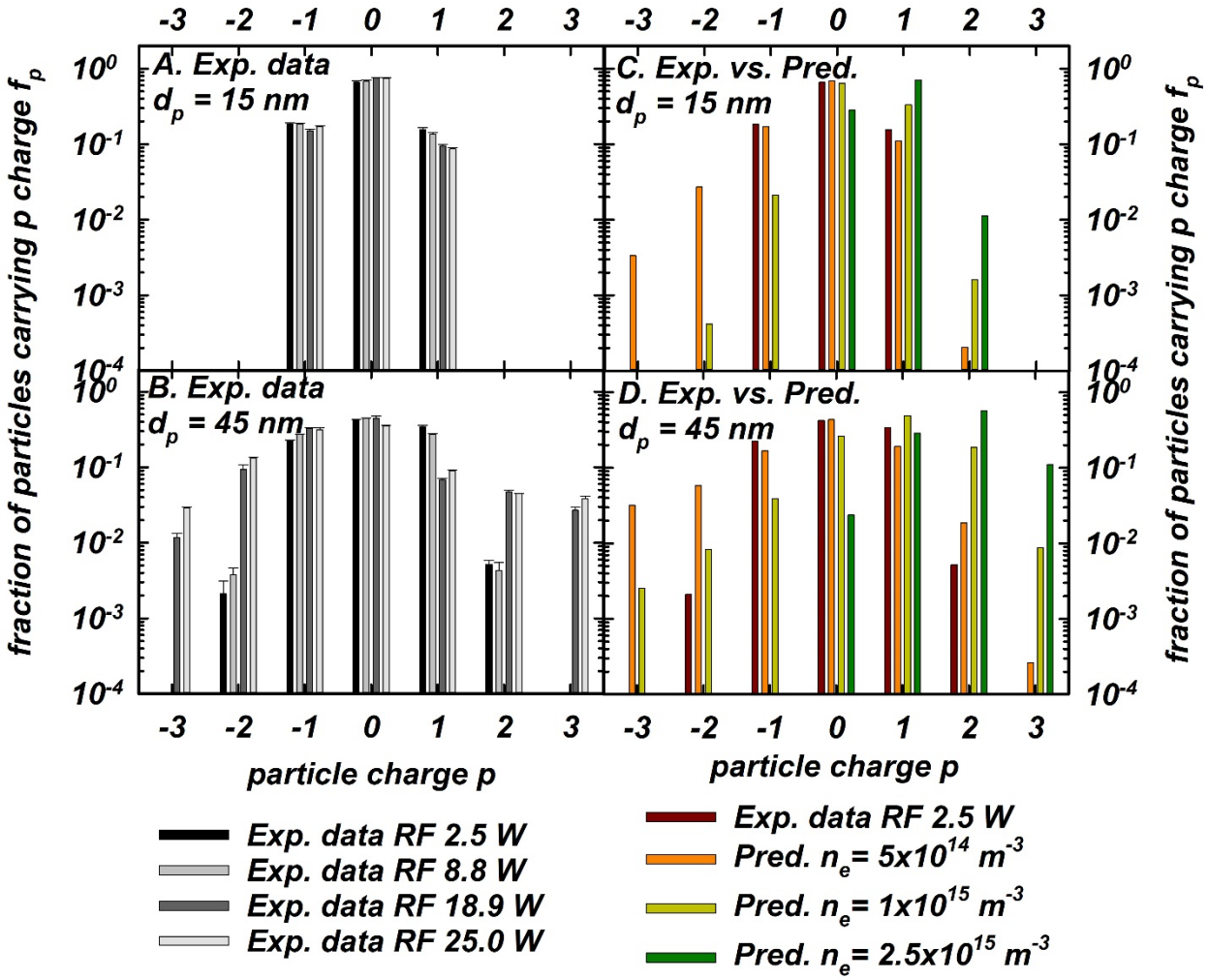

6. Conclusions

From this modeling study, we draw the following conclusions:

1. The experimental data[40,41] on charging of grains, radius $0.6-1.3\,\mu m$ in the pressure regime of $20-150\,Pa$ in non-thermal DC discharges in neon, provided a test of the LD-based β_i model (eq. 6) in the parametric space of $76<\Psi_E<137, 42<S_D<189, 9<Kn_D<354$ (see Table S2-D, *SI*). The comparisons reveal excellent agreement (within $\pm 30\%$ nominally) of LD-based β_i model predictions for pressures up to $150\,Pa$ and earlier comparisons of aerosol diffusion charging data for spheres[57] and non-spherical shapes[56] (fractal aggregates, cylinders, linear chains) in the parametric space of $-47<\Psi_E<47,\ 0.05<Kn_D<59$ yielded excellent agreement (within $\pm 20\%$ overall) as well. This establishes the LD-based β_i modelling approach[56-59,65,88] to describe diffusion charging of particles in aerosols and dusty plasmas alike in the limit of dilute space charge concentration and the absence of external electric fields. Future work examining other complexities of particle charging such as charge fluctuations, external electric fields, particle material (finite ε_r) and high space charge effect (wherein the nominal inter-ion separation $n_i^{-\frac{1}{3}}$ is comparable to the particle radius a_p: $n_i^{-\frac{1}{3}}\sim a_p$) is necessary to improve the current state of the art. The LD methodology[98] has also been successfully applied for collision rate constant model development to describe other particles processes such as coagulation[89,105] of and vapor condensation[59,67] onto particles as well, and can be used to include stated aspects of particle charging.

2. This experimentally validated LD-based β_i model (eq. 6) is applied to describe particle charging in flow-through plasma afterglows taking into account the spatial variation of ions and electron concentrations in the experiments performed by Sharma et al. [23]. The comparisons reveal that the charge fractions are sensitive to ion/electron concentration at end of the plasma/beginning of the afterglow region and along with the axial gas temperature profile, it is recommended that future experimental measurements attempt to measure the same to enable precise modeling and control of particle charge in the afterglow. Experimentally[25,26], the use of additional biased electrodes has been reported to obtain control over the particle charge that can also be achieved by varying the concentration of free charges (ions and electrons) as well as the gas temperature.

3. Taken together, the comparisons with particle charge measurements in stationary as well as flow-through plasmas reveal that the Langevin Dynamics based particle-ion diffusion charging models[56,57,59,65,66] to be robust and reasonably accurate.

SUPPLEMENTARY INFORMATION (*SI*) AVAILABLE

Section S1: Regression equation for $\mu(0.01 < Kn_D \leq 2000, 0 < \Psi_E \leq 300, 0 < S_D < \infty)$ developed by extending the model of Chahl and Gopalakrishnan using additional simulations described in Section 2.1 of the main text.

Figure S1: Plots of the model parameter $\mu(Kn_D, \Psi_E, S_D)$ for $\Psi_E = 60$ (panel A), $\Psi_E = 100$ (panel B), $\Psi_E = 200$ (panel C), and $\Psi_E = 300$ (panel D) shown using data points for $S_D = 20$ (blue filled triangles), $S_D = 100$ (green filled squares) and $S_D = \infty$ (red filled circles) for $0.01 \leq Kn_D \leq 2000$. The regression fit (eq. 6b from the main text) is shown as dashed lines.

Figure S2: Plots of the % difference between H_{LD} and $H_{eq.4}$ defined as $\left(1 - \frac{H_{eq.6}}{H_{LD}}\right)\%$ for $\Psi_E = 60, 100, 200, 300$ for $S_D = 20, 100, \infty$ for $0.01 \leq Kn_D \leq 2000$. In each panel, reference lines at % difference levels of $\pm 10\%$ and $\pm 20\%$ are using black dashed lines. To be read in conjunction with Figure 1 from the main text that shows the non-dimensional particle-ion collision rate coefficient $H(Kn_D, \Psi_E, S_D)$.

Section S2: Experimental inputs used to compute grain charge for comparison with PK-4 experimental data

Section S3: Regression equation for $\mu\left(0.01 < Kn_D \leq 2000, 0 < \Psi_E \leq 60, 0 \leq \frac{\Psi_I}{|\Psi_E|} \leq 1\right)$ developed by Li et al.

ACKNOWLEDGEMENTS

Funding for this work was provided by US National Science Foundation (NSF) PHY Grant Award Number 1903432 under the Directorate of Mathematical & Physical Sciences and US Department of Energy Office of Science Grant Award Number DE-SC0021206 from the Office of Basic Energy Sciences. We thank the University of Memphis High Performance Computing Cluster for providing computational resources to carry out this research.

REFERENCES

[1] G. E. Morfill and A. V. Ivlev, Reviews of Modern Physics **81,** 1353 (2009).

[2] S. Khrapak and G. Morfill, Contributions to Plasma Physics **49,** 148 (2009).

[3] V. E. Fortov, A. V. Ivlev, S. A. Khrapak, A. G. Khrapak, and G. E. Morfill, Physics Reports **421,** 1 (2005).

[4] U. R. Kortshagen, R. M. Sankaran, R. N. Pereira, S. L. Girshick, J. J. Wu, and E. S. Aydil, Chemical Reviews **116,** 11061 (2016).

[5] H. Kersten and M. Wolter, in *Introduction to Complex Plasmas*; *Vol. 59*, edited by M. Bonitz, N. Horing, and P. Ludwig (2010), p. 395.

[6] A. Bouchoule and L. Boufendi, Plasma Sources Science and Technology **2,** 204 (1993).

[7] L. Boufendi, A. Plain, J. P. Blondeau, A. Bouchoule, C. Laure, and M. Toogood, Applied Physics Letters **60,** 169 (1992).

[8] D. J. Kim and K. S. Kim, Korean Journal of Chemical Engineering **19,** 495 (2002).

[9] A. Melzer, M. Himpel, H. Krüger, M. Mulsow, and S. Schütt, Plasma Physics and Controlled Fusion **61,** 014029 (2018).

[10] N. H. Abuyazid, X. Chen, D. Mariotti, P. Maguire, C. J. Hogan, and R. M. Sankaran, Plasma Sources Science and Technology **29,** 075011 (2020).

[11] X. Chen, S. Ghosh, D. T. Buckley, R. Mohan Sankaran, and C. J. Hogan, Journal of Physics D: Applied Physics **51,** 335203 (2018).

[12] E. O. Knutson and K. T. Whitby, Journal of Aerosol Science **6,** 443 (1975).

[13] S. C. Wang and R. C. Flagan, Aerosol Science and Technology **13,** 230 (1990).

[14] L. Wörner, A. V. Ivlev, L. Couëdel, P. Huber, M. Schwabe, T. Hagl, M. Mikikian, L. Boufendi, A. Skvortsov, A. M. Lipaev, V. I. Molotkov, O. F. Petrov, V. E. Fortov, H. M. Thomas, and G. E. Morfill, Physics of Plasmas **20,** 123702 (2013).

[15] B. Layden, L. Couedel, A. A. Samarian, and L. Boufendi, IEEE Transactions on Plasma Science **39,** 2764 (2011).

[16] I. I. Filatova, F. M. Trukhachev, and N. I. Chubrik, Plasma Physics Reports **37,** 1042 (2011).

[17] L. Couëdel, A. Mezeghrane, A. A. Samarian, M. Mikikian, Y. Tessier, M. Cavarroc, and L. Boufendi, Contributions to Plasma Physics **49,** 235 (2009).

[18] L. Couëdel, A. A. Samarian, M. Mikikian, and L. Boufendi, Physics of Plasmas **15,** 063705 (2008).

[19] L. Couëdel, A. A. Samarian, M. Mikikian, and L. Boufendi, EPL (Europhysics Letters) **84,** 35002 (2008).

[20] L. Couëdel, M. Mikikian, L. Boufendi, and A. A. Samarian, Physical Review E **74,** 026403 (2006).

[21] I. Adamovich, S. D. Baalrud, A. Bogaerts, P. J. Bruggeman, M. Cappelli, V. Colombo, U. Czarnetzki, U. Ebert, J. G. Eden, P. Favia, D. B. Graves, S. Hamaguchi, G. Hieftje, M. Hori, I. D. Kaganovich, U. Kortshagen, M. J. Kushner, N. J. Mason, S. Mazouffre, S. M. Thagard, H. R. Metelmann, A. Mizuno, E. Moreau, A. B. Murphy, B. A. Niemira, G. S. Oehrlein, Z. L. Petrovic, L. C. Pitchford, Y. K. Pu, S. Rauf, O. Sakai, S. Samukawa, S. Starikovskaia, J. Tennyson, K. Terashima, M. M. Turner, M. C. M. van de Sanden, and A. Vardelle, Journal of Physics D: Applied Physics **50,** 323001 (2017).

[22] M. Boy van, H. Judith van, P. Ton, B. Paul, M. W. K. Gerrit, and J. Beckers, Plasma Sources Science and Technology (2021).

[23] G. Sharma, N. Abuyazid, S. Dhawan, S. Kshirsagar, R. M. Sankaran, and P. Biswas, Journal of Physics D: Applied Physics **53,** 245204 (2020).

[24] B. van Minderhout, T. Peijnenburg, P. Blom, J. M. Vogels, G. M. W. Kroesen, and J. Beckers, Journal of Physics D: Applied Physics **52,** 32LT03 (2019).

[25] B. van Minderhout, J. C. A. van Huijstee, B. Platier, T. Peijnenburg, P. Blom, G. M. W. Kroesen, and J. Beckers, Plasma Sources Science and Technology **29,** 065005 (2020).
[26] S. Dhawan, A. Vidwans, G. Sharma, N. H. Abuyazid, R. Mohan Sankaran, and P. Biswas, Aerosol Science and Technology **54,** 1249 (2020).
[27] X. Chen, T. Seto, U. R. Kortshagen, and C. J. Hogan, Powder Technology **373,** 164 (2020).
[28] V. Vekselman, Y. Raitses, and M. N. Shneider, Physical Review E **99,** 063205 (2019).
[29] S. Z. Jiang, X. N. Hou, J. Kong, L. S. Matthews, T. W. Hyde, F. Huang, and M. J. Wang, Chinese Physics Letters **35** (2018).
[30] S. Dap, R. Hugon, D. Lacroix, L. de Poucques, J. L. Briancon, and J. Bougdira, Physics of Plasmas **20** (2013).
[31] S. Dap, D. Lacroix, R. Hugon, L. de Poucques, J. L. Briancon, and J. Bougdira, Physical Review Letters **109** (2012).
[32] J. Winter, J. Berndt, S. H. Hong, E. Kovacevic, I. Stefanovic, and O. Stepanovic, Plasma Sources Science & Technology **18** (2009).
[33] Y. A. Mankelevich, M. A. Olevanov, A. F. Pal, T. V. Rakhimova, A. N. Ryabinkin, A. O. Serov, and A. V. Filippov, Plasma Physics Reports **35,** 191 (2009).
[34] B. M. Annaratone, Y. Elskens, C. Arnas, T. Antonova, H. M. Thomas, and G. E. Morfill, New Journal of Physics **11** (2009).
[35] R. J. Anthony, E. Thimsen, J. Johnson, S. A. Campbell, and U. Kortshagen, MRS Proceedings **892,** 0892 (2011).
[36] P. Cernetti, R. Gresback, S. A. Campbell, and U. Kortshagen, Chemical Vapor Deposition **13,** 345 (2007).
[37] L. Mangolini, E. Thimsen, and U. Kortshagen, Nano Letters **5,** 655 (2005).
[38] Z. Shen, T. Kim, U. Kortshagen, P. H. McMurry, and S. A. Campbell, Journal of Applied Physics **94,** 2277 (2003).
[39] S. A. Khrapak, P. Tolias, S. Ratynskaia, M. Chaudhuri, A. Zobnin, A. Usachev, C. Rau, M. H. Thoma, O. F. Petrov, V. E. Fortov, and G. E. Morfill, EPL (Europhysics Letters) **97,** 35001 (2012).
[40] S. A. Khrapak, S. V. Ratynskaia, A. V. Zobnin, A. D. Usachev, V. V. Yaroshenko, M. H. Thoma, M. Kretschmer, H. Höfner, G. E. Morfill, O. F. Petrov, and V. E. Fortov, Physical Review E **72,** 016406 (2005).
[41] S. Ratynskaia, S. Khrapak, A. Zobnin, M. H. Thoma, M. Kretschmer, A. Usachev, V. Yaroshenko, R. A. Quinn, G. E. Morfill, O. Petrov, and V. Fortov, Physical Review Letters **93,** 085001 (2004).
[42] M. Mamunuru, R. Le Picard, Y. Sakiyama, and S. L. Girshick, Plasma Chemistry and Plasma Processing **37,** 701 (2017).
[43] P. Romain Le and L. G. Steven, Journal of Physics D: Applied Physics **49,** 095201 (2016).
[44] R. Le Picard, A. H. Markosyan, D. H. Porter, S. L. Girshick, and M. J. Kushner, Plasma Chemistry and Plasma Processing **36,** 941 (2016).
[45] C. Larriba-Andaluz and S. L. Girshick, Plasma Chemistry and Plasma Processing**,** 1 (2016).
[46] M. S. Sodha, S. Srivastava, and S. K. Mishra, Journal of Plasma Physics **77,** 529 (2011).
[47] J. C. E. Sten and K. I. Nikoskinen, Journal of Electrostatics **35,** 267 (1995).
[48] I. V. Lindell, J. C. E. Sten, and K. I. Nikoskinen, Radio Science **28,** 319 (1993).
[49] J. R. Brock, Journal of Applied Physics **41,** 843 (1970).
[50] D. Keefe, P. J. Nolan, and J. A. Scott, Proceedings of the Royal Irish Academy. Section A: Mathematical and Physical Sciences **66,** 17 (1967).
[51] A. Michau, P. Swaminathan, S. Longo, and K. Hassouni, Plasma Physics and Controlled Fusion **62,** 014002 (2019).
[52] B. Santos, L. Cacot, C. Boucher, and F. Vidal, Plasma Sources Science and Technology **28,** 045002 (2019).

[53] Y. S. Mayya and B. K. Sapra, Journal of Aerosol Science **33,** 817 (2002).
[54] D. D. Huang, J. H. Seinfeld, and K. Okuyama, Journal of Colloid and Interface Science **141,** 191 (1991).
[55] W. A. Hoppel and G. M. Frick, Aerosol Science and Technology **5,** 1 (1986).
[56] L. Li and R. Gopalakrishnan, Journal of Aerosol Science **151,** 105678 (2021).
[57] L. Li, H. S. Chahl, and R. Gopalakrishnan, Journal of Aerosol Science **140,** 105481 (2020).
[58] R. Gopalakrishnan, T. Thajudeen, H. Ouyang, and C. J. Hogan, Journal of Aerosol Science **64,** 60 (2013).
[59] H. Ouyang, R. Gopalakrishnan, and C. J. Hogan, The Journal of Chemical Physics **137,** 064316 (2012).
[60] X. Lopez-Yglesias and R. C. Flagan, Aerosol Science and Technology **47,** 688 (2013).
[61] J. E. Allen, Physica Scripta **45,** 497 (1992).
[62] H. M. Mott-Smith and I. Langmuir, Physical Review **28,** 727 (1926).
[63] J. Goree, Plasma Sources Science and Technology **3,** 400 (1994).
[64] J. Goree, Physical Review Letters **69,** 277 (1992).
[65] H. S. Chahl and R. Gopalakrishnan, Aerosol Science and Technology **53,** 933 (2019).
[66] R. Gopalakrishnan, M. J. Meredith, C. Larriba-Andaluz, and C. J. Hogan, Journal of Aerosol Science **63,** 126 (2013).
[67] R. Gopalakrishnan, T. Thajudeen, and C. J. Hogan, Journal of Chemical Physics **135,** 054302 (2011).
[68] N. A. Fuchs, Geofis. Pura Appl. **51,** 185 (1963).
[69] F. Galli and U. R. Kortshagen, Ieee Transactions on Plasma Science **38,** 803 (2010).
[70] M. Gatti and U. Kortshagen, Physical Review E **78,** 046402 (2008).
[71] M. Lampe and G. Joyce, Physics of Plasmas **22,** 023704 (2015).
[72] A. V. Zobnin, A. D. Usachev, O. F. Petrov, and V. E. Fortov, Physics of Plasmas **15,** 043705 (2008).
[73] S. A. Khrapak and G. E. Morfill, Physics of Plasmas **15,** 114503 (2008).
[74] S. A. Khrapak, B. A. Klumov, and G. E. Morfill, Physical Review Letters **100** (2008).
[75] L. G. D'Yachkov, A. G. Khrapak, and S. A. Khrapak, Journal of Experimental and Theoretical Physics **106,** 166 (2008).
[76] I. H. Hutchinson and L. Patacchini, Physics of Plasmas **14,** 013505 (2007).
[77] L. G. D'Yachkov, A. G. Khrapak, S. A. Khrapak, and G. Morfill, Physics of Plasmas **14** (2007).
[78] S. A. Khrapak, G. E. Morfill, A. G. Khrapak, and L. G. D'yachkov, Physics of Plasmas **13,** 052114 (2006).
[79] S. A. Khrapak and G. E. Morfill, Physics of Plasmas **13,** 104506 (2006).
[80] F. Iza and J. K. Lee, Journal of Vacuum Science & Technology A: Vacuum, Surfaces, and Films **24,** 1366 (2006).
[81] S. A. Maiorov, Plasma Physics Reports **31,** 690 (2005).
[82] N. Crouseilles, P. Degond, and M. Lemou, Journal of Computational Physics **203,** 572 (2005).
[83] V. V. Yaroshenko, B. M. Annaratone, S. A. Khrapak, H. M. Thomas, G. E. Morfill, V. E. Fortov, A. M. Lipaev, V. I. Molotkov, O. F. Petrov, A. I. Ivanov, and M. V. Turin, Physical Review E **69,** 066401 (2004).
[84] D. Trunec, M. Holík, P. Kudrna, O. Bilyk, A. Marek, R. Hippler, and M. Tichý, Contributions to Plasma Physics **44,** 577 (2004).
[85] A. A. Lushnikov and M. Kulmala, Physical Review E **70,** 046413 (2004).
[86] M. Lampe, R. Goswami, Z. Sternovsky, S. Robertson, V. Gavrishchaka, G. Ganguli, and G. Joyce, Physics of Plasmas **10,** 1500 (2003).
[87] M. Lampe, V. Gavrishchaka, G. Ganguli, and G. Joyce, Physical Review Letters **86,** 5278 (2001).
[88] R. Gopalakrishnan and C. J. Hogan, Physical Review E **85,** 026410 (2012).

[89] R. Gopalakrishnan and C. J. Hogan, Aerosol Science and Technology **45,** 1499 (2011).
[90] J. E. Daugherty, R. K. Porteous, M. D. Kilgore, and D. B. Graves, Journal of Applied Physics **72,** 3934 (1992).
[91] I. L. Semenov, S. A. Khrapak, and H. M. Thomas, Physics of Plasmas **22,** 053704 (2015).
[92] S. K. Friedlander, *Smoke, Dust, and Haze: Fundamentals of Aerosol Dynamics*, Vol. null (2000).
[93] O. S. Vaulina, A. Y. Repin, and O. F. Petrov, Plasma Physics Reports **32,** 485 (2006).
[94] R. Gopalakrishnan, P. H. McMurry, and C. J. Hogan, Aerosol Science and Technology **49,** 1181 (2015).
[95] R. Gopalakrishnan and C. J. Hogan, Jr., Phys Rev E Stat Nonlin Soft Matter Phys **85,** 026410 (2012).
[96] H. Ouyang, R. Gopalakrishnan, and C. J. Hogan, Jr., J Chem Phys **137,** 064316 (2012).
[97] S. Chandrasekhar, Reviews of Modern Physics **15,** 1 (1943).
[98] V. Suresh and R. Gopalakrishnan, ((in review)).
[99] D. L. Ermak and H. Buckholz, Journal of Computational Physics **35,** 169 (1980).
[100] N. J. Kasdin, Journal of Guidance, Control, and Dynamics **18,** 114 (1995).
[101] V. Suresh, Z. Liu, and R. Gopalakrishnan, in *62nd Annual Meeting of the APS Division of Plasma Physics* (Virtual Conference, 2020).
[102] K. G. Xu and S. J. Doyle, Journal of Vacuum Science & Technology A **34,** 051301 (2016).
[103] K. B. McAfee, D. Sipler, and D. Edelson, Physical Review **160,** 130 (1967).
[104] D. J. Rader, Journal of Aerosol Science **21,** 161 (1990).
[105] T. Thajudeen, R. Gopalakrishnan, and C. J. Hogan, Aerosol Science and Technology **46** (2012).

Modeling nanoparticle charge distribution in the afterglow of non-thermal plasmas and comparison with measurements

Vikram Suresh[#], Li Li[#], Joshua Redmond Go Felipe & Ranganathan Gopalakrishnan[*]

Department of Mechanical Engineering, The University of Memphis, Memphis TN, USA

Supplementary Information

[#]Equally contributing authors
*Corresponding author: rgplkrsh@memphis.edu;
Tel: 1-626-319-6187, Fax: 1-901-678-4180

SUPPLEMENTARY INFORMATION (*SI*) AVAILABLE

Section S1: Regression equation for $\mu(0.01 < Kn_D \leq 2000, 0 < \Psi_E \leq 300, 0 < S_D < \infty)$ developed by extending the model of Chahl and Gopalakrishnan [1] using additional simulations described in Section 2.1 of the main text.

Figure S1: Plots of the model parameter $\mu(Kn_D, \Psi_E, S_D)$ for $\Psi_E = 60$ (panel A), $\Psi_E = 100$ (panel B), $\Psi_E = 200$ (panel C), and $\Psi_E = 300$ (panel D) shown using data points for $S_D = 20$ (blue filled triangles), $S_D = 100$ (green filled squares) and $S_D = \infty$ (red filled circles) for $0.01 \leq Kn_D \leq 2000$. The regression fit (eq. 6b from the main text) is shown as dashed lines.

Figure S2: Plots of the % difference between H_{LD} and $H_{eq.4}$ defined as $\left(1 - \frac{H_{eq.6}}{H_{LD}}\right)\%$ for $\Psi_E = 60, 100, 200, 300$ for $S_D = 20, 100, \infty$ for $0.01 \leq Kn_D \leq 2000$. In each panel, reference lines at % difference levels of $\pm 10\%$ and $\pm 20\%$ are using black dashed lines. To be read in conjunction with Figure 1 from the main text that shows the non-dimensional particle-ion collision rate coefficient $H(Kn_D, \Psi_E, S_D)$.

Section S2: Experimental inputs used to compute grain charge for comparison with PK-4 experimental data

Section S3: Regression equation for $\mu\left(0.01 < Kn_D \leq 2000, 0 < \Psi_E \leq 60, 0 \leq \frac{\Psi_I}{|\Psi_E|} \leq 1\right)$ developed by Li et al. [2]

Section S1: Regression equation for $\mu(Kn_D, \Psi_E, S_D)$

The parameter $\mu(Kn_D, \Psi_E, S_D)$ presented in Figure S1, is summarized for $0 < \Psi_E \leq 300, 0 < S_D < \infty, Kn_D \leq 2000$.

$$\mu(Kn_D, \Psi_E, S_D) = \frac{C}{A}\left(1 + k\frac{\ln Kn_D - B}{A}\right)^{-\frac{1}{k}-1} \exp\left(-\left(1 + k\frac{\ln Kn_D - B}{A}\right)^{-\frac{1}{k}}\right), k \neq 0$$

$$A(\Psi_E, S_D) = 2.8\alpha(\Psi_E, S_D)$$

$$\alpha(\Psi_E, S_D) = \begin{cases} 0, & S_D < 10 \\ 1 + \dfrac{a_1(\Psi_E)}{S_D^{a_2(\Psi_E)}}, & 10 \leq S_D \leq 1000 \\ 1, & S_D > 1000 \end{cases}$$

$$a_1 = -0.003998\Psi_E - 0.3929$$

$$a_2 = 0.001431\Psi_E + 0.1791$$

$$B(\Psi_E, S_D) = \beta_1(\Psi_E)\beta_2(\Psi_E, S_D)$$

$$\beta_1(\Psi_E) = b_1 \exp(-b_2\Psi_E) + b_3 \log(1 + b_4\Psi_E)$$

$$\beta_2(\Psi_E, S_D) = \begin{cases} 0, & S_D < 10 \\ 1 + \dfrac{b_5(\Psi_E)}{S_D^{b_6(\Psi_E)}}, & 10 \leq S_D \leq 1000 \\ 1, & S_D > 1000 \end{cases}$$

$$b_1 = 1.76, b_2 = 4.956, b_3 = 0.6109, b_4 = 2.925$$

$$b_5 = (3.23 \times 10^{-5})\Psi_E^2 - 0.008786\Psi_E - 1.557$$

$$b_6 = -0.0006008\Psi_E + 0.5654$$

$$C(\Psi_E, S_D) = \left(c_1\Psi_E^{c_2} + c_3\right)\gamma(\Psi_E, S_D)$$

$$\gamma(\Psi_E, S_D) = \begin{cases} 0, & S_D < 10 \\ 1 + \dfrac{c_4(\Psi_E)}{S_D^{c_5(\Psi_E)}}, & 10 \leq S_D \leq 1000 \\ 1, & S_D > 1000 \end{cases}$$

$$c_1 = 32.64, c_2 = 0.1362, c_3 = -33.2, c_4 = -2.4$$

$$c_5 = 0.9898\psi_E^{-0.164}$$

$$k(\Psi_E, S_D) = (k_1\Psi_E^{k_2} + k_3)$$

$$k_1 = -0.03425, k_2 = 0.4494, k_3 = 0.0864$$

Figure S1: Plots of the model parameter $\mu(Kn_D, \Psi_E, S_D)$ for $\Psi_E = 60$ (panel A), $\Psi_E = 100$ (panel B), $\Psi_E = 200$ (panel C), and $\Psi_E = 300$ (panel D) shown using data points for $S_D = 20$ (blue filled triangles), $S_D = 100$ (green filled squares) and $S_D = \infty$ (red filled circles) for $0.01 \leq Kn_D \leq 2000$. The regression fit (eq. 6b from the main text) is shown as dashed lines.

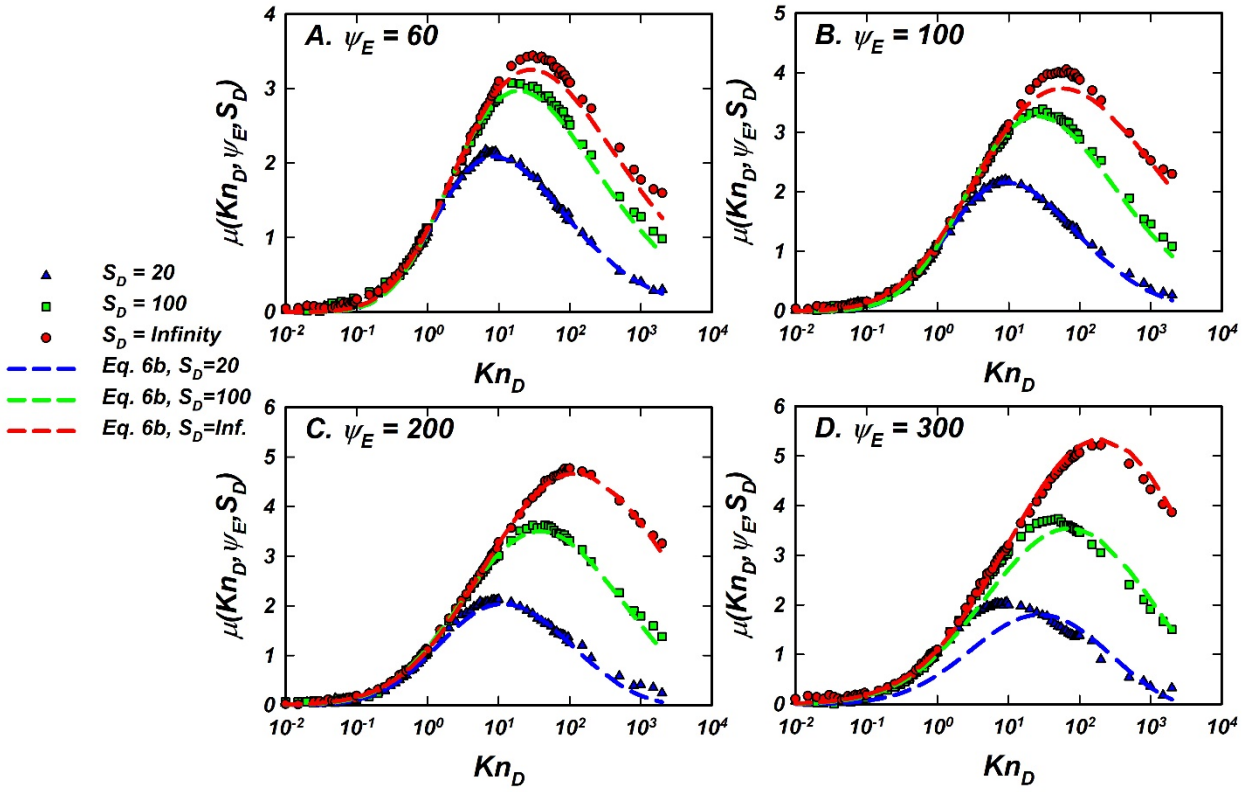

Figure S2: Plots of the % difference between H_{LD} and $H_{eq.4}$ defined as $\left(1-\frac{H_{eq.6}}{H_{LD}}\right)\%$ for $\Psi_E = 60, 100, 200, 300$ for $S_D = 20, 100, \infty$ for $0.01 \leq Kn_D \leq 2000$. In each panel, reference lines at % difference levels of $\pm 10\%$ and $\pm 20\%$ are using black dashed lines. To be read in conjunction with Figure 1 from the main text that shows the non-dimensional particle-ion collision rate coefficient $H(Kn_D, \Psi_E, S_D)$.

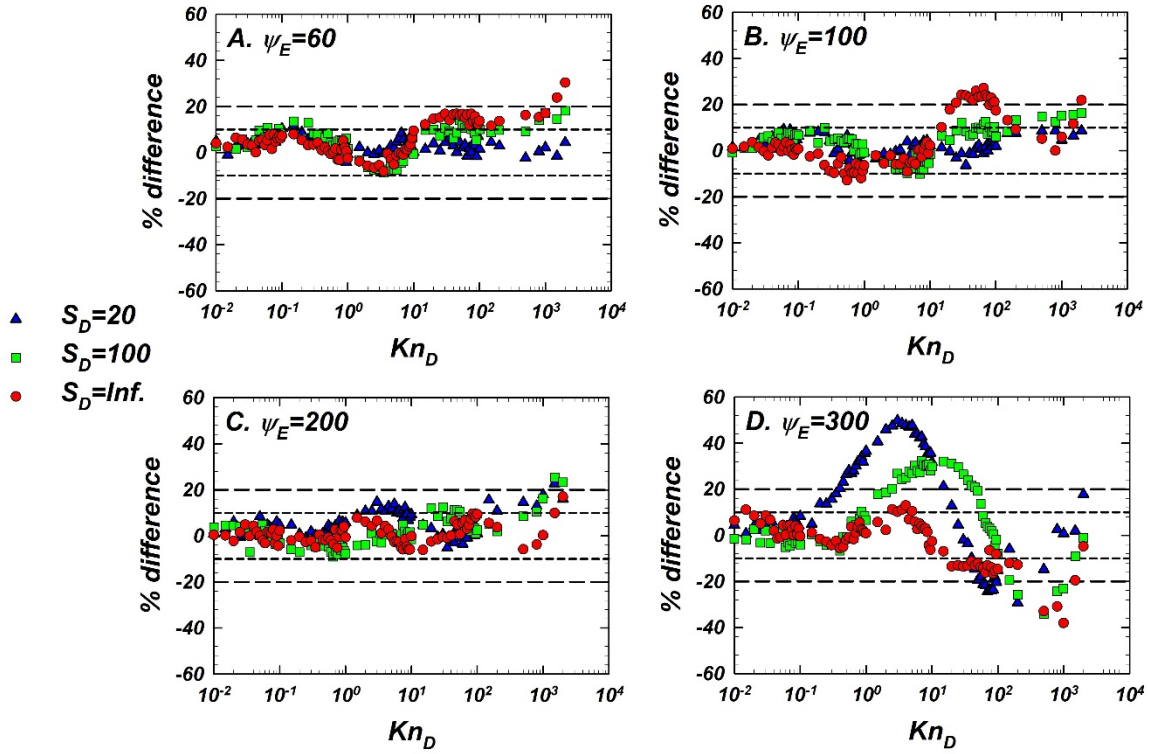

Section S2: Experimental inputs used to compute grain charge for comparison

The electrical mobility of Ne^+ ions in Ne is calculated using the reduced mobility equation that accounts for pressure and temperature dependence[3]:

$$\mu_{Ne^+} = \mu^r_{Ne^+}\left(\frac{760}{p_g}\right)\left(\frac{T_g}{273.16}\right)$$

Here, T_g is gas temperature in K and p_g is pressure in $Torr$, and $\mu^r_{Ne^+} = 4.15\,\frac{cm^2}{s.V}$ is zero-field reduced mobility. Other experimental inputs are summarized in Tables S2-A and S2-B; uncertainties are summarized in Table S2-C. Finally, the Ψ_E, Kn_D, S_D range covered by the experimental data is summarized in Table S2-D.

Table S2-A: Experimental inputs reported by Ratynskaia et al. [4] used for analysis.

Neutral gas pressure p_g	$p_g \in 20 - 100\ Pa$
Neutral gas temperature $k_B T_g$	$0.03\ eV$
Neutral gas molecule number concentration n_g	$n_g = \frac{p_g}{k_B T_g}$
Ion elementary charge z_i	+1
Ion temperature $k_B T_i$	$0.03\ eV$
Ion molar mass M_i	$0.020 \frac{kg}{mole}$
Ion mass m_i	$m_i = 3.32 \times 10^{-26} kg$
Ion Debye length λ_{Di}	$\lambda_{Di} = \sqrt{\frac{\varepsilon_o k_B T_i}{n_i z_i^2 e^2}}$
Electron number concentration n_e	Regression of data presented in [4] $n_e = \left(0.9 + 0.03 p_g\right) \times 10^8\ cm^{-3}$
Electron temperature $k_B T_e$	Regression of data presented in [4] $k_B T_e = \left(8.3 - 0.02 p_g\right)\ eV$
Electron Debye length λ_{De}	$\sqrt{\frac{\varepsilon_o k_B T_e}{n_e z_e^2 e^2}}$
Axial electric field E_z	Regression of data presented in [4] $E_z = 2.1 \frac{V}{cm}$
Grain material density ρ_d	$1.51 \frac{g}{cm^3}$
Grain radius a_p	$0.6\ \mu m$
Grain number concentration n_d	$4 \times 10^5 cm^{-3}$

Table S2-B: Experimental inputs reported by Khrapak et al. [5] used for data analysis.

Neutral gas pressure p_g	$p_g \in 20 - 150\ Pa$
Neutral gas temperature $k_B T_g$	$0.03\ eV$
Neutral gas molecule number concentration n_g	$n_g = \frac{p_g}{k_B T_g}$
Ion elementary charge z_i	+1
Ion temperature $k_B T_i$	$0.03\ eV$
Ion molar mass M_i	$0.020 \frac{kg}{mole}$
Ion mass m_i	$m_i = 3.32 \times 10^{-26} kg$
Ion Debye length λ_{Di}	$\lambda_{Di} = \sqrt{\frac{\varepsilon_o k_B T_i}{n_i z_i^2 e^2}}$
Electron number concentration n_e	Regression of data presented in [5] $n_e = \left(0.9 + 0.03 p_g\right) \times 10^8\ cm^{-3}$
Electron temperature $k_B T_e$	Regression of data presented in [5] $k_B T_e = \left(8.3 - 0.02 p_g\right)\ eV$
Electron Debye length λ_{De}	$\sqrt{\frac{\varepsilon_o k_B T_e}{n_e z_e^2 e^2}}$
Axial electric field E_z	Regression of data presented in [5] $E_z = 2.1 \frac{V}{cm}$
Grain material density ρ_d	$1.51 \frac{g}{cm^3}$
Grain radius a_p	$0.6\ \mu m, 1.0\ \mu m, 1.3\ \mu m$
Grain number concentration n_d	$4 \times 10^5 cm^{-3}$

Table S2-C: Uncertainties in measurements reported by PK-4 charging studies[4,5]

Electron number concentration	30% in [5]
Electron temperature	15%
Particle drift velocity	$10 - 15\ \%$
Electric field	$5 - 10\ \%$
Particle number concentration	50%

Uncertainty estimation:

$$\frac{(\Delta Z_p)_{total}}{Z_p(T_e, n_e)} = \sqrt{\left[\frac{\Delta Z_p(\Delta T_e)}{Z_p(T_e, n_e)}\right]^2 + \left[\frac{\Delta Z_p(\Delta n_e)}{Z_p(T_e, n_e)}\right]^2}$$

$$\Delta Z_p(\Delta T_e) = Z_p(T_e + \Delta T_e) - Z_p(T_e - \Delta T_e)$$

$$\Delta Z_p(\Delta n_e) = Z_p(n_e + \Delta n_e) - Z_p(n_e - \Delta n_e)$$

Upper bound curve: $Z_p(T_e, n_e) + (\Delta Z_p)_{total}$

Lower Bound curve: $Z_p(T_e, n_e) - (\Delta Z_p)_{total}$

Table S2-D: Range of Ψ_E, S_D, Kn_D of the considered experimental studies[4,5]

	Ratynskaia et al. [4]		Khrapak et al. [5]					
	$a_p = 0.6\ \mu m$		$0.6\ \mu m$		$1.0\ \mu m$		$1.3\ \mu m$	
	Min.	Max.	Min.	Max.	Min.	Max.	Min.	Max.
Ψ_E	83.6	121.8	76.3	137.1	85.0	128.4	96.5	125.9
S_D	108.6	175.1	92.3	188.9	55.4	113.3	42.6	87.2
Kn_D	45.2	232.6	29.5	353.6	14.3	184.2	9.4	129.6

Section S3: Regression equation for $\mu\left(0.01 < Kn_D \leq 2000, 0 < \Psi_E \leq 60, 0 \leq \frac{\Psi_I}{|\Psi_E|} \leq 1\right)$ developed by Li et al. [2]

For $0 < \Psi_E \leq 60, 0 \leq \frac{\Psi_I}{\Psi_E} \leq 1, Kn_D \leq 2000$:

$$\mu(Kn_D, \Psi_E, \Psi_I) = \frac{C}{A}\left(1 + k\frac{\log Kn_D - B}{A}\right)^{-\frac{1}{k}-1} \exp\left(-\left(1 + k\frac{\log Kn_D - B}{A}\right)^{-\frac{1}{k}}\right), k \neq 0$$

Regression fit	Fit coefficients (with 95% C. I.)	
$A(\Psi_E, \Psi_I) = 2.5$		
$B(\Psi_E, \Psi_I) = \beta_1(\Psi_E)\beta_2\left(\frac{\Psi_I}{\Psi_E}\right)$ $\beta_1(\Psi_E) = b_1\exp(-b_2\Psi_E) + b_3\log(1 + b_4\Psi_E)$ $\beta_2\left(\frac{\Psi_I}{\Psi_E}\right) = b_5\exp\left(-b_6\frac{\Psi_I}{\Psi_E}\right) + b_7\exp\left(-b_8\frac{\Psi_I}{\Psi_E}\right)$	$b_1 = 4.528$ $b_2 = 1.088$ $b_3 = 0.7091$ $b_4 = 1.537$	$b_5 = 0.0681$ $b_6 = 11.8439$ $b_7 = 0.9304$ $b_8 = 0.0591$
$C(\Psi_E, \Psi_I) = (c_1\Psi_E^{c_2} + c_3)\gamma\left(\frac{\Psi_I}{\Psi_E}\right)$ $\gamma\left(\frac{\Psi_I}{\Psi_E}\right) = c_4\exp\left(-c_5\frac{\Psi_I}{\Psi_E}\right) + c_6\exp\left(-c_7\frac{\Psi_I}{\Psi_E}\right)$	$c_1 = 11.36$ $c_2 = 0.272$ $c_3 = -10.33$	$c_4 = 0.1087$ $c_5 = 11.9384$ $c_6 = 0.8880$ $c_7 = 0.1311$
$k(\Psi_E, \Psi_I) = -0.061$		

To calculate the enhancement factors $\eta_c(\Psi_E, \Psi_I), \eta_f(\Psi_E, \Psi_I)$, the reader is referred to the Supplemental Information file published along with prior articles:

Li et al. [2]: https://www.sciencedirect.com/science/article/abs/pii/S0021850219305853

Li and Gopalakrishnan [6]:
https://www.sciencedirect.com/science/article/abs/pii/S0021850220301646

References

[1] H. S. Chahl and R. Gopalakrishnan, Aerosol Science and Technology **53,** 933 (2019).
[2] L. Li, H. S. Chahl, and R. Gopalakrishnan, Journal of Aerosol Science **140,** 105481 (2020).
[3] W. McDaniel and E. A. Mason, *The mobility and diffusion of ions in gases* (Wiley, 1973).
[4] S. Ratynskaia, S. Khrapak, A. Zobnin, M. H. Thoma, M. Kretschmer, A. Usachev, V. Yaroshenko, R. A. Quinn, G. E. Morfill, O. Petrov, and V. Fortov, Physical Review Letters **93,** 085001 (2004).
[5] S. A. Khrapak, S. V. Ratynskaia, A. V. Zobnin, A. D. Usachev, V. V. Yaroshenko, M. H. Thoma, M. Kretschmer, H. Höfner, G. E. Morfill, O. F. Petrov, and V. E. Fortov, Physical Review E **72,** 016406 (2005).
[6] L. Li and R. Gopalakrishnan, Journal of Aerosol Science **151,** 105678 (2021).